A Modeling Study of the Severe Afternoon Thunderstorm Event at Taipei on 14 June 2015: The Roles of Sea Breeze, Microphysics, and Terrain

Jyong-En MIAO and Ming-Jen YANG

Department of Atmospheric Sciences, National Taiwan University, Taiwan

(Manuscript received 1 July 2019, in final form 27 October 2019)

Abstract

On 14 June 2015, a severe afternoon thunderstorm event developed within the Taipei Basin, which produced intense rainfall (with a rainfall rate of 131 mm h^{-1}) and urban-scale flooding. Cloud-resolving simulations using the Weather Research and Forecasting (WRF) model were performed to capture reasonably well the onset of the sea breeze and the development and evolution of this afternoon thunderstorm system. The WRF model had four nested grids (with the finest grid size of 0.5 km) in the horizontal direction and 55 layers in the vertical direction to explicitly resolve the deep convection over complex terrain.

It was found that convection was initiated both by the sea breeze at foothill and by the upslope wind at the mountain peak. Convective available potential energy (CAPE) was increased from 800 to 3200 J kg^{-1} with abundant moisture transport by the sea breeze from 08 to 12 LST, fueling large thermodynamic instability for the development of the afternoon thunderstorm. Strong convergence between the sea breeze and cold-air outflow triggered further development of intense convection, resulting in heavy rainfall over Taipei City.

Microphysics sensitivity experiments showed that evaporative cooling played a major role in the propagation of cold-air outflow and the production of heavy rainfall within the basin plain (terrain height < 100 m), whereas melting cooling played a minor role. The terrain-removal experiment indicated that the local topography of Mount Datun at the coastal region may produce the channel effect through the Danshui River Valley, intensify sea-breeze circulation, and transport more moisture. This terrain-induced modification of sea breeze circulation made its dynamic and thermodynamic characteristics more favorable for convection development, resulting in a stronger afternoon thunderstorm system with heavy rainfall within Taipei City.

Keywords afternoon thunderstorm; heavy rainfall; sea breeze; cold pool; terrain effect

Citation Miao, J.-E., and M.-J. Yang, 2020: A modeling study of the severe afternoon thunderstorm event at Taipei on 14 June 2015: The roles of sea breeze, microphysics, and terrain. *J. Meteor. Soc. Japan*, **98**, 129–152, doi:10.2151/jmsj.2020-008.

1. Introduction

During the summer months with weak synoptic forcing, most of the convection in Taiwan is associated with afternoon thunderstorms (Chen et al. 2014). The local circulations of sea–land breeze and mountain–valley flows are essential in triggering afternoon thunderstorms in Taiwan (Johnson and Bresch 1991; Chen and Li 1995; Kerns et al. 2010). Jou (1994) indicated that most of the thunderstorms in northern Taiwan were initiated on the mountain peaks and propagated down the terrain slope and brought heavy rain to the Taipei Basin (TB).

Corresponding author: Ming-Jen Yang, Depertment of Atmospheric Sciences, National Taiwan University, No.1 Sec. 4 Roosevelt Road, Taipei, 10617, Taiwan
E-mail: mingjen@as.ntu.edu.tw
J-stage Advance Published Date: 16 November 2019

Modification of thunderstorm outflow can occur when the storm outflows collide with the sea breeze near the base of the mountains surrounding the TB. As a result, most afternoon thunderstorms occurred along the windward slopes of the mountains in Taiwan, rather than at higher elevations farther inland (Johnson and Bresch 1991; Jou 1994; Chen et al. 2001)

Radar reflectivity climatology indicated that the maximum thunderstorm frequency in northern Taiwan was during 1500–1600 LST (Lin et al. 2011). Both radar reflectivity and cloud-to-ground lightning data showed that the highest frequency of thunderstorms over northern Taiwan occurred along the lower mountain slopes approximately parallel to the ridges of the Snow Mountain Range.

In Chen et al. (2007), the afternoon thunderstorm (ATS) occurrence over the TB was attributed to the interaction of the sea breeze with the urban heat island (UHI) in the central urban area and mountains south of the TB. In the initial phase of ATS, the moist and unstable flow was transported by the sea-breeze circulation into the TB. The interaction of the sea breeze with the Taipei UHI and the orography south of the TB could trigger the onset of the ATS convection and rainfall at about 1400 LST over the mountain slopes (Chen et al. 2014). Later, the ATS convection and precipitation would spread farther northward to cover the whole TB and to the mountains south and north of the TB.

However, observations alone may not be sufficient to elucidate all dynamic and thermodynamic processes of the sea breeze related to heavy rainfall. Numerical simulations are frequently used to further understand the physical mechanisms. For example, Baker et al. (2001) coupled the atmosphere and land surface models to identify the roles of initial soil moisture, coastline curvature, and land-breeze circulations on sea-breeze-initiated precipitation over central Florida. Chen et al. (2015, 2016) investigated diurnal variations of the land–sea breeze and its related precipitation over southern China using the convection-permitting simulations and observation data. Wang and Kirshbaum (2017) conducted idealized simulations to examine the impact of orography on sea-breeze strength and frontogenesis over tropical islands. Huang et al. (2019) investigated the role of the sea breeze in the production of heavy rainfall over the coastal metropolitan city of Guangzhou, China. Kuo and Wu (2019) conducted idealized simulations to investigate the precipitation hotspots of ATSs over the TB.

Because of the limitations in observations, several key questions remain to be further explored, which are the focus of this modeling study: What are the spatial structure and evolution of the sea-breeze circulation over the TB for the thunderstorm system associated with torrential rainfall? What microphysical processes are essential in determining the propagation of precipitation-induced cold pool associated with the thunderstorm system? What kind of impacts does the local terrain at the coastal region have on the sea breeze and its related rainfall? In this study, high-resolution simulations using the Weather Research and Forecasting (WRF) model are conducted to address these questions. Through control and sensitivity experiments, the impacts of local mountains and the cold pool dynamics (induced by evaporative cooling of raindrops and melting cooling of graupel) will be investigated.

2. Case overview

Figure 1 shows the synoptic environment for the ATS system over the TB on 14 June 2015 and the local topography around the TB. It is clear from Fig. 1a that the southerly wind prevailed over Taiwan for the typical prefrontal condition ahead of a surface cold front. Figure 1b shows that the ridge associated with the subtropical high-pressure system at 500-hPa level extended over the Taiwan Island. The sounding at Banchiao station (46692) in the TB (Fig. 1c; see Fig. 2a for the sounding location) indicated weak convective instability, with a convective available potential energy (CAPE) of only 1076 J kg^{-1}, for the thermodynamic condition in the morning (0800 LST or 0000 UTC). There was no significant synoptic-scale forcing for this ATS event over the TB. Figure 1d shows the terrains surrounding the TB, and the highest peak of Mount Datun is 1092 m.

Figure 2 shows the evolution of the ATS system observed by the RCWF radar located at Mount Wufen. The hourly observed winds at Danshui, Shilin, Chungho, Keelung, Shizi, and Wenshan weather stations from 1300 LST to 1600 LST are shown in Fig. 2. Processing of radar data was done using the NCAR Radx and Solo3 programs, and the radar data were analyzed using the Py-ART software (Helmus and Collis 2016). At 1302 LST (Fig. 2a), convection occurred along the mountain peak south of the TB. The wind barbs at 1302 LST illustrated that the sea breeze penetrated inland from the northwestern coast (Danshui) and northeastern coast (Keelung). At 1331–1400 LST (Figs. 2b, c), scattered convection occurred along the mountain slope south of the TB. Convection also appeared over the central basin where the commercial districts were located. The wind at Chungho station

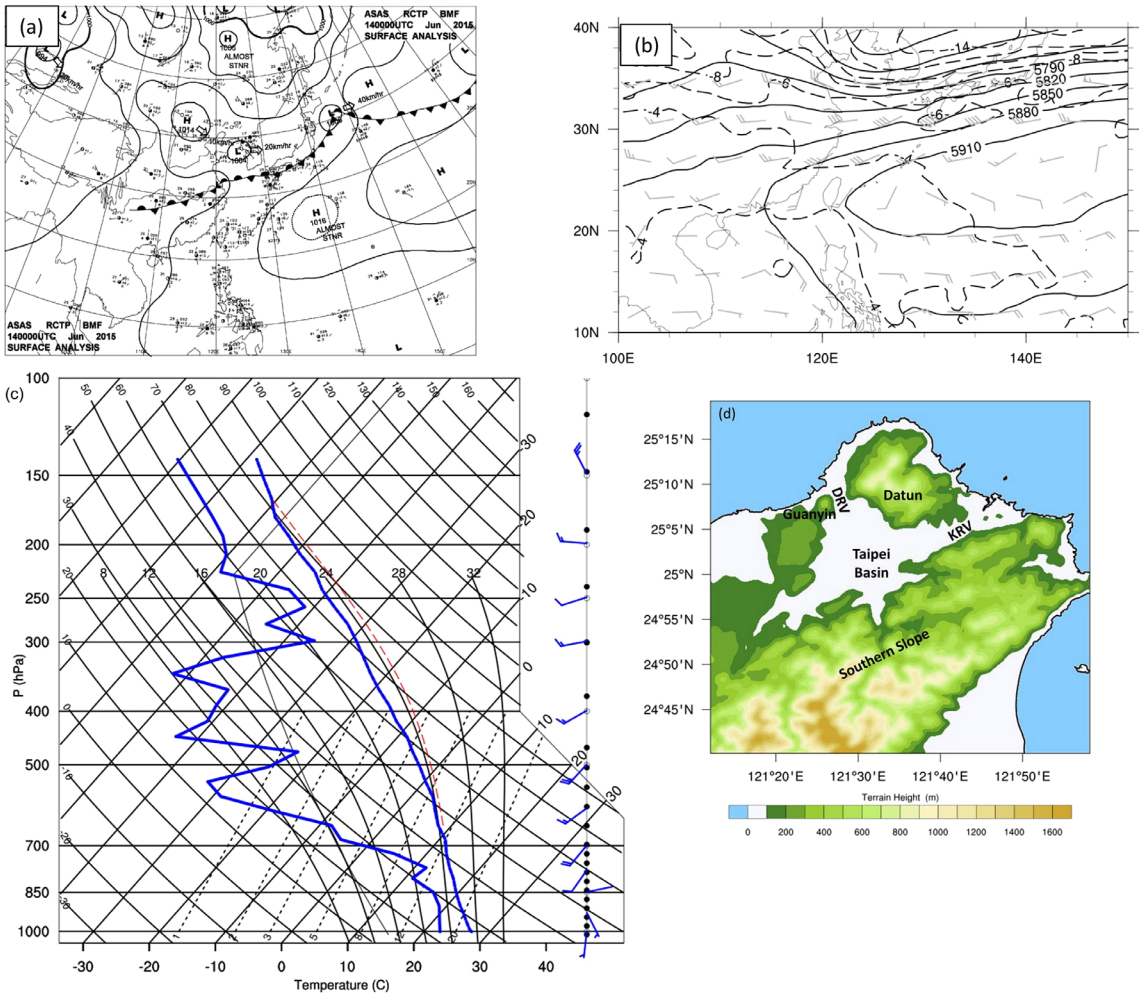

Fig. 1. Synoptic condition at 0000 UTC (0800 LST) 14 June 2015: (a) CWB surface analysis map; (b) 500-hPa map from the ERA-Interim reanalysis with the geopotential height in solid contours, temperature in dashed contours, and horizontal wind in wind barbs (full barb is 10 kts, and half barb is 5 kts); (c) CWB sounding of temperature and dew point (blue line) at Banchiao station. The location of Banchiao sounding station is shown in Fig. 2a. (d) Taipei Basin domain with terrain elevations plotted (colored; in units of meter). Mount Datun, Mount Guanyin, and Southern Slope are labeled. Danshui River Valley and Keelung River Valley are denoted by DRV and KRV, respectively.

turned east-southeasterly at 1400 LST, which might be related to the cold pool produced by the convection at the central basin. At 1435–1459 LST (Figs. 2d, e), convection over the southern slope and central basin gradually merged into the thunderstorm complex with a large area of strong reflectivity (greater than 40 dBZ). The wind at Shilin station turned southerly at 1459 LST. At 1522–1559 LST (Figs. 2f, g), the thunderstorm complex propagated northward and gradually weakened. Note that the wind at the weather stations turned southerly or calm at 1600 LST. Convectively generated cold pool appeared to account for the shift of surface winds from northerly (at 1302 LST) to southerly (at 1559 LST) over the TB.

3. Numerical model and experimental design

3.1 WRF configuration

The Advanced Research version of the Weather Research and Forecasting model (WRF-ARW version 3.4.1; Skamarock et al. 2008) was used to simulate this TB ATS event from 1200 UTC 13 June to 1200 UTC 14 June 2015, with a forecast period of 24 h.

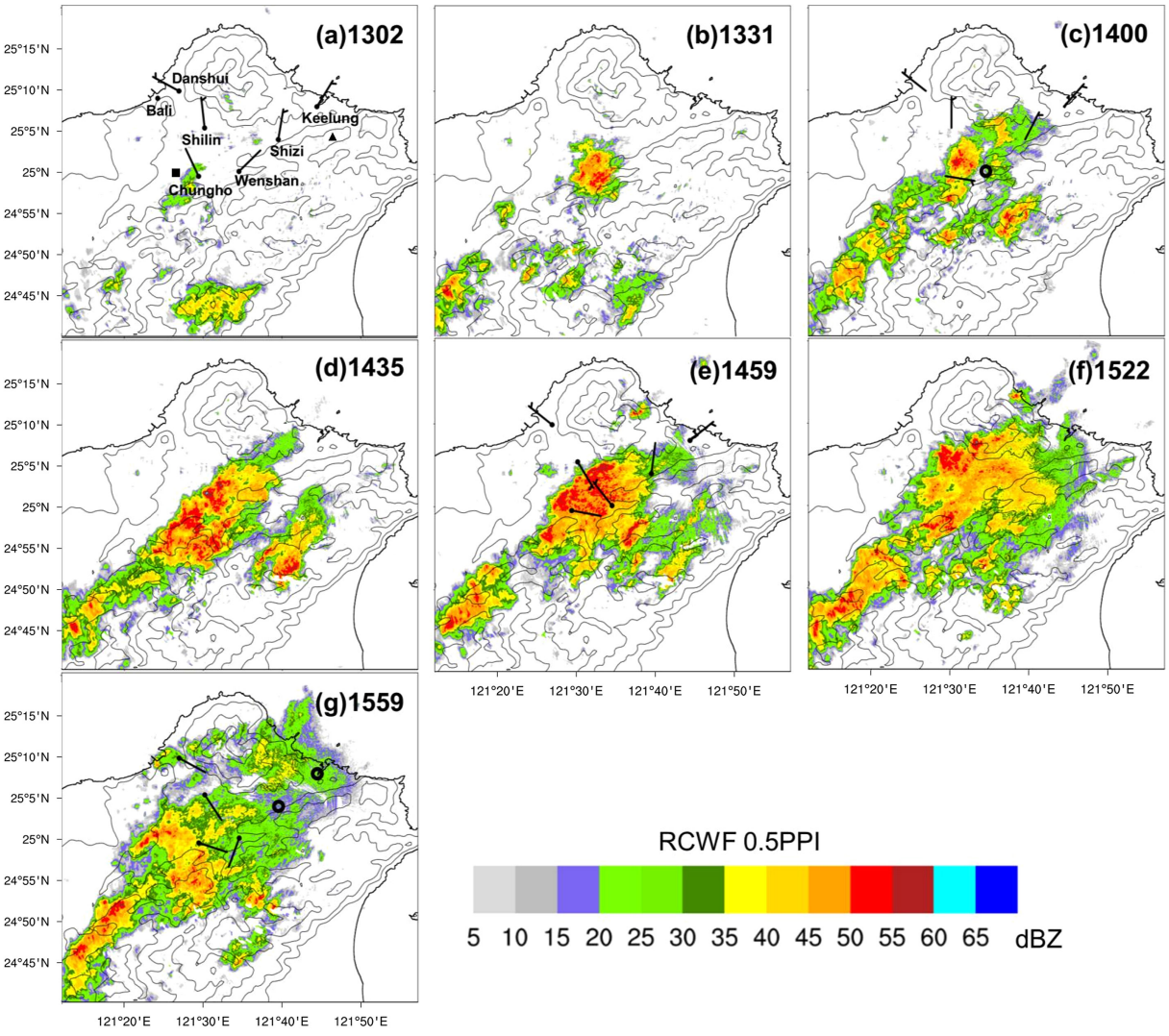

Fig. 2. PPI maps of radar reflectivity (in units of dBZ) at 0.5° elevation angle observed by the RCWF radar: (a) 1302 LST, (b) 1331 LST, (c) 1400 LST, (d) 1435 LST, (e) 1459 LST, (f) 1522 LST, and (g) 1559 LST. The hourly observed winds at Danshui, Shilin, Chungho, Keelung, Shizi, and Wenshan weather stations are indicated in (a), (c), (e), and (g). Half barb is for a wind speed of 5 kts. A circle represents the calm condition (< 1 kt). The RCWF radar is labeled by the triangle in (a), and the square in (a) is the location of Banchiao sounding station. Terrain heights are contoured by black lines at 100, 300, 700, and 1300 m.

Four nested domains with horizontal grid sizes of 13.5, 4.5, 1.5, and 0.5 km, respectively, were used in the horizontal (Fig. 3). A two-way interaction between inner and outer grids was considered. Fifty-five eta (η) levels were used in the vertical, with a higher resolution within the planetary boundary layer (eight layers below 1-km height). The model top was at 20 hPa, and the time step for the outermost domain was 5 s.

The physical parameterization schemes used in the model include the Kain–Fritsch cumulus parameterization (Kain and Fritsch 1993), the WDM6 microphysics parameterization (Lim and Hong 2010), Rapid Radiative Transfer Model (RRTM) longwave radiation parameterization (Mlawer et al. 1997), Dudhia (1989) shortwave parameterization, and the Yonsei University (YSU) planetary boundary layer (PBL) parameterization (Hong and Pan 1996). Note that the cumulus scheme was used only in the outermost

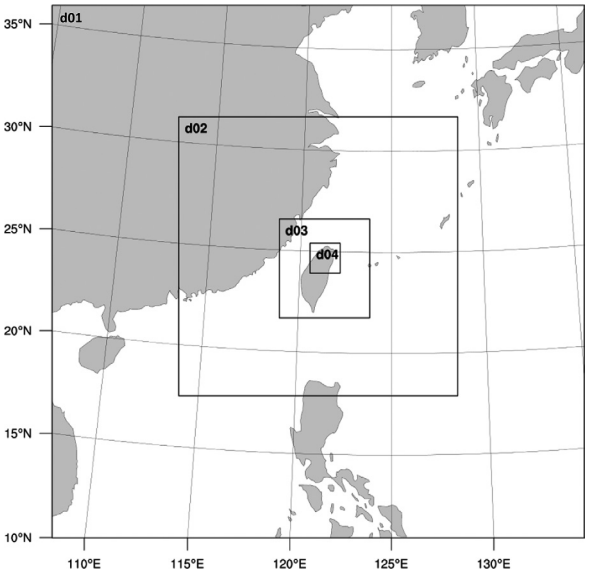

Fig. 3. Four nested domains (with horizontal grid sizes of 13.5, 4.5, 1.5, and 0.5 km) of the WRF model.

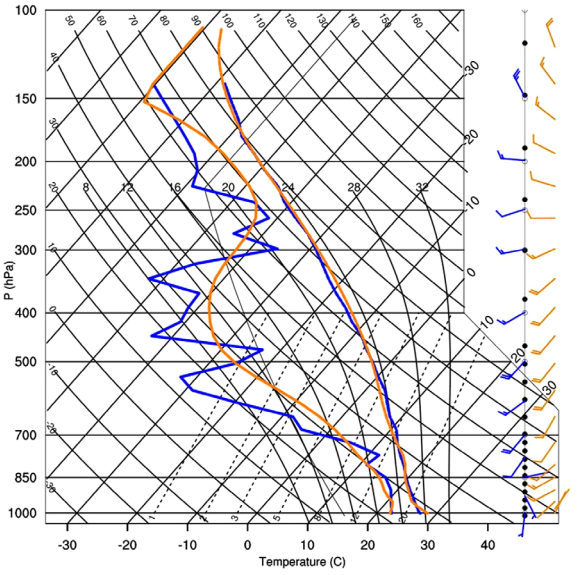

Fig. 4. A comparison between the simulated sounding (orange) and the observed (blue) at Banchiao sounding station (see Fig. 2a for its location) at 0800 LST 14 June 2015.

domain (with a grid size of 13.5 km), assuming that the grid sizes of other domains (with grid sizes of 4.5, 1.5, and 0.5 km, respectively) were fine enough to explicitly resolve convection. The WDM6 scheme is a double-moment microphysics scheme that predicts the mixing ratios of six categories of water species (water vapor, cloud droplets, cloud ice, snow, rain, and graupel) and the number concentrations of cloud and rainwater. The initial and boundary conditions were from the ERA-Interim dataset, which are updated every 6 h, with a latitude–longitude resolution of 0.75° (Dee et al. 2011).

3.2 Sensitivity experiments

The control (CNTL) and sensitivity experiments (NMLT, NEVP, and NDAT; Table 1) were designed to examine the impact of cold-pool dynamics and local terrain on the ATS system and related precipitation. All three sensitivity experiments had the same configuration as that of the CNTL, except that melting cooling of graupel was turned off in NMLT, evaporative cooling of rainwater was turned off in NEVP (Yang and Houze 1995), and local terrain of Mount Datun (with the highest peak of 1092 m) north of TB was removed in NDAT (cf. Figs. 17a, d). In the NMLT (NEVP) experiment, the graupel (rainwater) was allowed to melt (evaporate) without the feedback of latent cooling into the thermodynamic equation. Note that the microphysical sensitivity starts at 0800 LST 14 June 2015 (i.e., at the forecast time of 12 h) in NMLT and NEVP.

4. Model verification

The CNTL-simulated sounding was compared to the one observed at 0800 LST in Fig. 4, which indicated that the CNTL run reproduced reasonably well the observed profiles of temperature, moisture, and

Table 1. Design of control and sensitivity experiments.

Run	Initial time	Description
CNTL	20 LST 13 Jun. 2015	full physics
NMLT	20 LST 13 Jun. 2015	no melting cooling of graupel after 08 LST 14 June 2015
NEVP	20 LST 13 Jun. 2015	no evaporative cooling of rainwater after 08 LST 14 June 2015
NDAT	20 LST 13 Jun. 2015	full physics with Mt. Datun removal

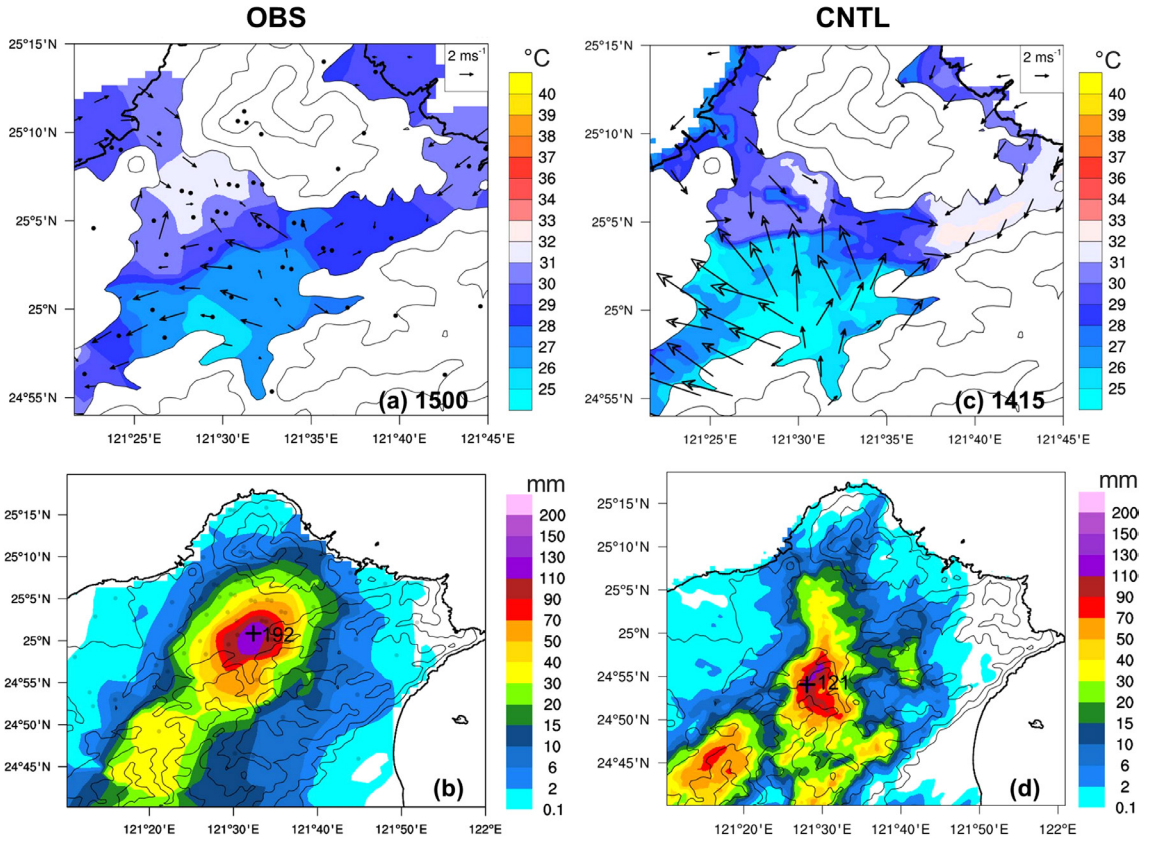

Fig. 5. A comparison between observation (OBS) and CNTL simulation of the afternoon thunderstorm event on 14 June 2015. Observation results are (a) surface (2 m AGL) temperature (in units of °C) and near-surface (6 m AGL) wind vectors at 1500 LST and (b) 6-h (1200–1800 LST) accumulated rainfall (in units of mm). Simulation results are (c) surface (2 m) temperature (in units of °C) and near-surface (10 m) wind vectors at 1415 LST and (d) 6-h (1200–1800 LST) accumulated rainfall (in units of mm). Black dots in (a) are locations of automatic weather stations, and blue dots in (b) are locations of rain gauge stations. Cross symbols in (b) and (d) are the observed and simulated locations of the maximum accumulated rainfall, and numbers are the corresponding maximum rainfalls. Terrain heights are contoured at 100, 300, 700, and 1300 m.

horizontal winds, except for the weak wind below 850 hPa. The wind errors in PBL were probably due to small-scale turbulent processes that were not properly represented in the model and due to subgrid variations in the terrain and land use (Hanna and Yang 2001). Figure 4 is shown here to indicate that, before the sea breeze penetrated the TB, the regional-scale environment was realistically simulated, including the deep dry air between 700 hPa and 300 hPa, the conditional instability with weak CAPE (885 J kg^{-1} in CNTL sounding and 1076 J kg^{-1} in observed sounding), and the southwesterly between 850 hPa and 300 hPa.

Figure 5 shows the comparison between observation analysis (left panels) and CNTL simulation (right panels). Note that a 45-min time difference between the observation (Fig. 5a) and simulation (Fig. 5c) was used to adjust the timing difference of the movement of the simulated convergence line between the sea breeze and thunderstorm outflow to the observation. Precipitation over the south of TB (Fig. 2d) reduced the surface temperature to 25°C, and the temperature near the TB center was 27–28°C (Figs. 5a, c), consistent with the observational analysis of Jou et al. (2016). Both the observation (Fig. 5a) and simulation (Fig. 5c) show that the sea breeze from the ocean and cold-air outflow associated with the precipitation south of TB converged near the center of Taipei City. Figures 5b and 5d show that the spatial distribution of 6-h (1200–1800 LST) accumulated rainfall was simulated by the WRF model reasonably well, although the

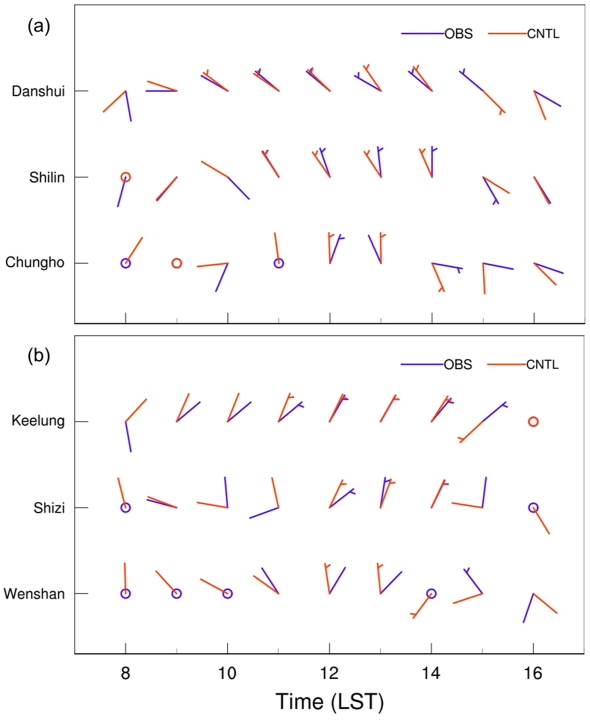

Fig. 6. (a) A comparison between the observed surface wind (purple) and the simulated (orange) at Danshui, Shilin, and Chungho stations. Half barb is 5 kts. A circle represents the calm condition (< 1 kt). (b) As in (a) but for Keelung, Shizi, and Wenshan stations.

position of the simulated rainfall maximum was 10 km southwest to the observed position and the simulated maximum magnitude (121 mm) was 63 % of the observed magnitude (192 mm). The error in peak rainfall amount may be due to the underestimation of low-level moisture in the model (Fig. 7).

The simulated surface wind is compared to those observed at Danshui, Shilin, and Chungho weather stations in Fig. 6a, which shows the inland penetration of the sea breeze from the northwestern coast (Danshui). The simulated onset time of the sea breeze (≥ 5 kts) at Danshui station was 1000 LST, approximately 1 h earlier than the observation. After onset, the observed and simulated sea breeze passed through Shilin at 1100 LST and through Chungho at 1200 LST. Despite the timing error, the CNTL simulation captured reasonably well the propagation of the sea breeze from the northwestern coast (Danshui) to the southern basin plain (Chungho). Moreover, the CNTL simulation showed that northerly wind shifted to southeasterly in the afternoon because of the cold-air outflows produced by convection.

The simulated surface wind is compared to those observed at Keelung, Shizi, and Wenshan weather stations in Fig. 6b, which shows the inland penetration of the sea breeze from the northeastern coast (Keelung). The observed and simulated onset time of the sea breeze (≥ 5 kts) at Keelung was 1100 LST. After onset, the observed and simulated sea breeze passed through Shizi and Wenshan stations at about 1200 LST. The errors of wind speed and direction at Wenshan station might be associated with local complex orography (Liu et al. 2008) because the passage of the sea breeze from Keelung was mostly over mountains. Despite the presence of errors in wind speed and direction, the CNTL simulation captured reasonably well the sea breeze which propagated from the northeastern coast (Keelung) to the southern basin plain (Wenshan). Moreover, the CNTL run reproduced the observation that the northerly wind shifted to the southerly wind in the afternoon because of the cold-air outflows generated by convection.

The simulated water vapor pressure is compared to those observed at Bali, Shilin, Chungho, Keelung, Shizi, and Wenshan stations in Fig. 7. Unfortunately, the observed humidity data at Danshui were not available, so we used the data from the nearby Bali station (see Fig. 2a for their locations). The diurnal variation of the observed and simulated 2-m water vapor pressure was similar, but the simulated value is slightly smaller than the observed. Both observation and simulation indicate that water vapor increased after the passage of the sea breeze, except for Keelung, which might be associated with local topography.

Figure 8 shows the evolution of the simulated radar reflectivity at 1500-m height from 1200 LST to 1500 LST. As compared to those shown in Fig. 2, the CNTL simulation reproduced reasonably well the evolution of the ATS system and its propagation from the southern slope to the central basin, except that the convective cell occurred at the center of TB (cf. Figs. 2b, 8b), which might be subjected to aerosol and UHI effects (Chen et al. 2014; Miao and Yang 2018).

It is encouraging to see that the initiation locations of the isolated convection at the mountain peak (cf. Figs. 8a, 2a) and scattered convection over the mountain slope (cf. Figs. 8b, 2b) were well simulated. Furthermore, the simulated scattered convection over the southern slope merged into the thunderstorm complex and then propagated to the central basin as in the observations (cf. Figs. 8d–f, 2d–f), although the simulated thunderstorm occurred about 1 h earlier than the observation. The reason for the early timing

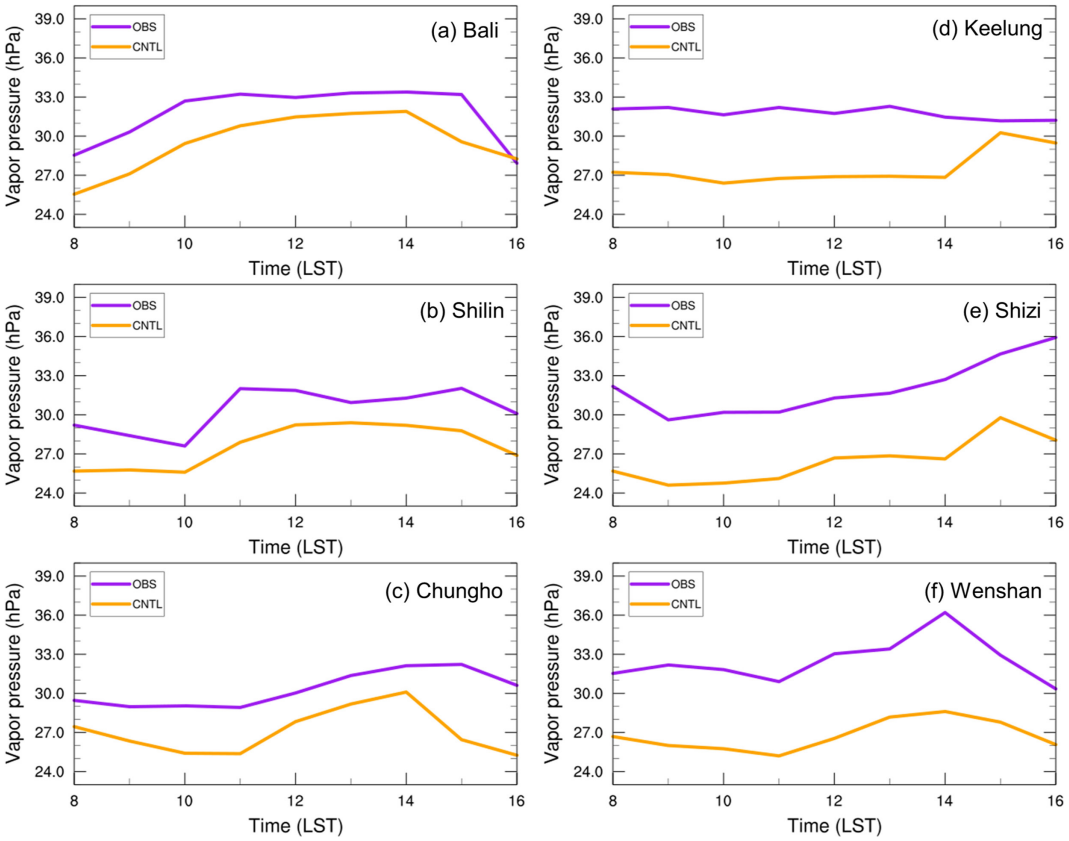

Fig. 7. A comparison of hourly 2-m vapor-pressure time series between the observed (purple) and the simulated (orange) at (a) Bali, (b) Shilin, (c) Chungho, (d) Keelung, (e) Shizi, and (f) Wenshan stations.

of the simulated convection initiation is not certain, which might be associated with deficiency in solar heating and turbulence mixing in the boundary layer parameterization and deserves further investigation in future studies.

To sum up, despite some deficiency in detailed features, we may state that the CNTL simulation captures reasonably well the evolution of the ATS system and sea breeze circulation, as represented by radar reflectivity and surface observations. Of particular relevance to the convective development is that the model reproduces the enhanced convergence produced by the sea breeze and cold-air outflow over the central basin, where Taipei's commercial districts are located. Given the general agreement between the observation and CNTL simulation, we can examine the model results in more detail.

5. Numerical model results

5.1 CNTL experiment

Figure 9 shows the hourly evolution of the sea breeze over the TB from 1000 to 1400 LST. The sea breeze began to establish at the northwestern and northeastern coasts at 1000 LST (Fig. 9a). With an increase in temperature contrast between inland and ocean surface (not shown), the sea breeze extends further inland through the central basin and to the southern foothill at 1100–1300 LST (Figs. 9b–d). It is clear that the sea breeze transported abundant moisture from the ocean surface to the inland region, modifying the near-surface thermodynamic characteristics at the central basin and southern foothill. Note that the sea breeze from Danshui (SBD) brought more moisture than the sea breeze from Keelung (SBK).

Figure 10 displays the simulated soundings at 0800, 1100, and 1200 LST at Banchiao station (see Fig. 2a for the sounding location) to examine the evolution of the thermodynamic condition within the TB. As shown in Fig. 4, the Banchiao sounding at 0800 LST indicated a weak CAPE of only 885 J kg^{-1}. As the surface layer was heated by solar radiation, the sounding at 1100 LST indicated a well-mixed PBL with a depth

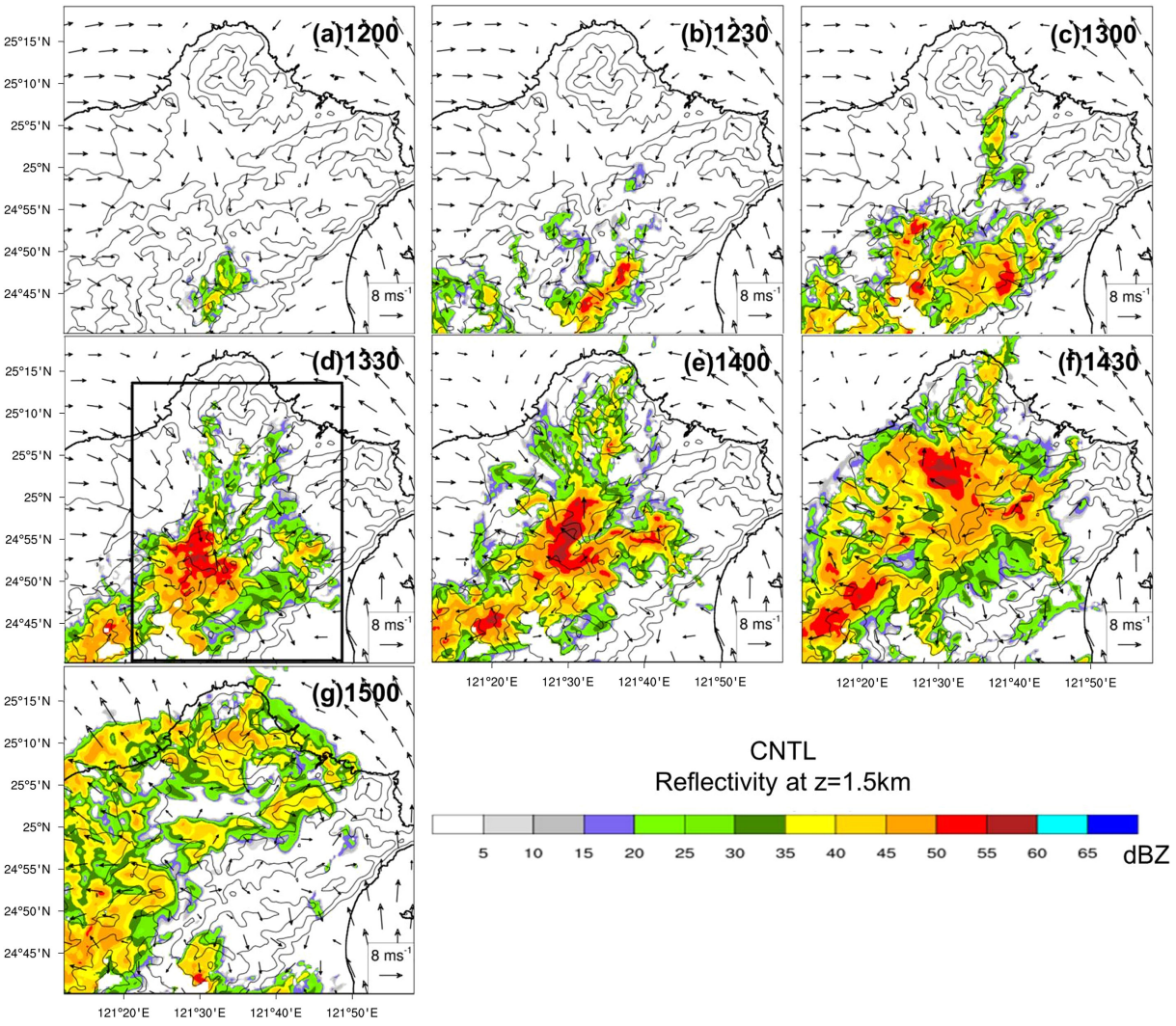

Fig. 8. Horizontal cross sections of 1500-m radar reflectivity (colored; in units of dBZ) and 10-m wind vectors from the CNTL simulation: (a) 1200 LST, (b) 1230 LST, (c) 1300 LST, (d) 1330 LST, (e) 1400 LST, (f) 1430 LST, and (g) 1500 LST. Black line is for the terrain height contoured at 100, 300, 700, and 1300 m. Bold box in (d) is the rectangular area of 60 km by 45 km for the time series calculations in Fig. 20.

of 1.5 km and a moderate CAPE of 1833 J kg^{-1}. Moreover, the wind below 1 km turned northerly because of the approach of SBD (Fig. 9b). After that, as the SBD passed through Banchiao station at noon (Fig. 9c), the Banchiao sounding at 1200 LST indicated that the PBL layer was more humid than 1 h before and the depth of the northerly wind increased to 1.3 km. Note that the CAPE increased dramatically from 1833 J kg^{-1} at 1100 LST to 3268 J kg^{-1} at 1200 LST because of the increase in boundary layer moisture.

Following Tompkins (2001) and Feng et al. (2015), buoyancy b is calculated using the formula

$$b = g\frac{(\theta_p - \overline{\theta_p})}{\overline{\theta_p}}, \quad (1)$$

where g is the gravitational acceleration and the overbar indicates the domain mean within the TB area (with a size of 60 km by 45 km; see the bold box in Fig. 8d). The virtual potential temperature θ_p is defined as

$$\theta_p = \theta(1 + 0.608q_v - q_c - q_r), \quad (2)$$

where θ is the potential temperature and q_v, q_c, and q_r

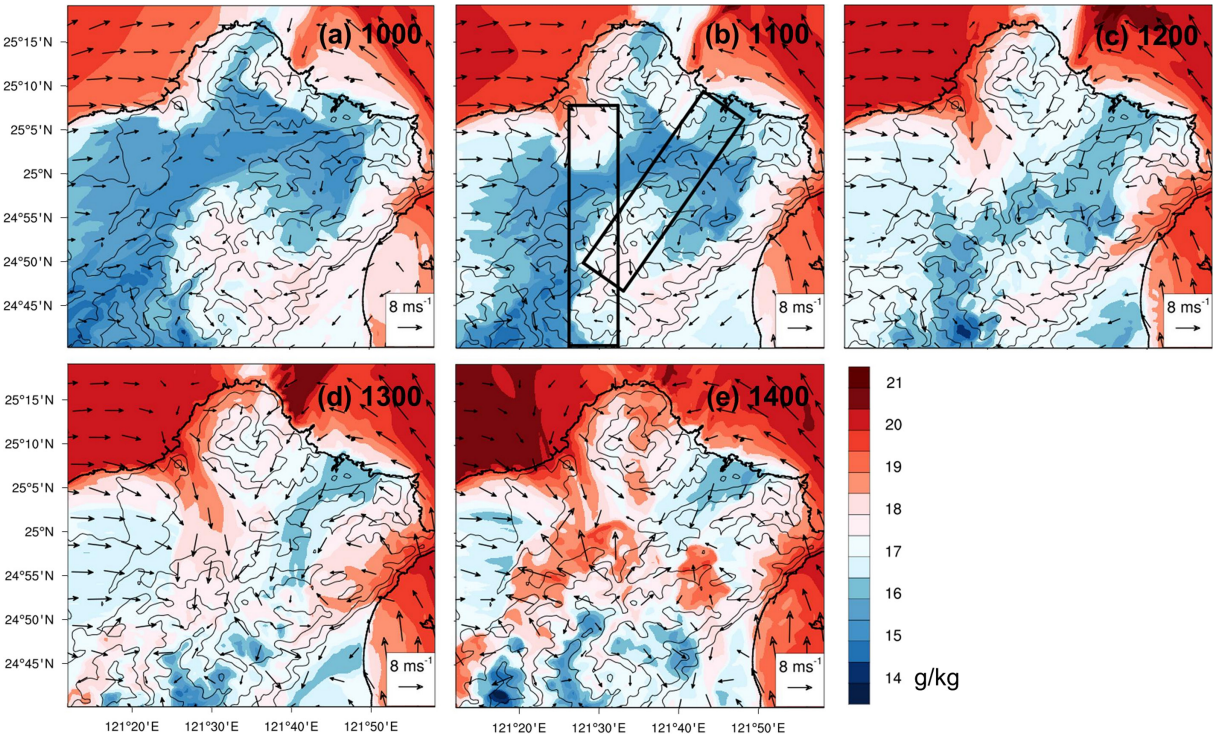

Fig. 9. Horizontal cross sections of 35-m water vapor mixing ratio (colored; in units of g kg^{-1}) and 35-m wind vectors from the CNTL simulation: (a) 1000 LST, (b) 1100 LST, (c) 1200 LST, (d) 1300 LST, and (e) 1400 LST. Black line is for the terrain height contoured at 100, 300, 700, and 1300 m. The vertical cross sections in Figs. 11 and 12 are along the N–S box in (b), and those in Figs. 13 and 14 are along the NE–SW box in (b).

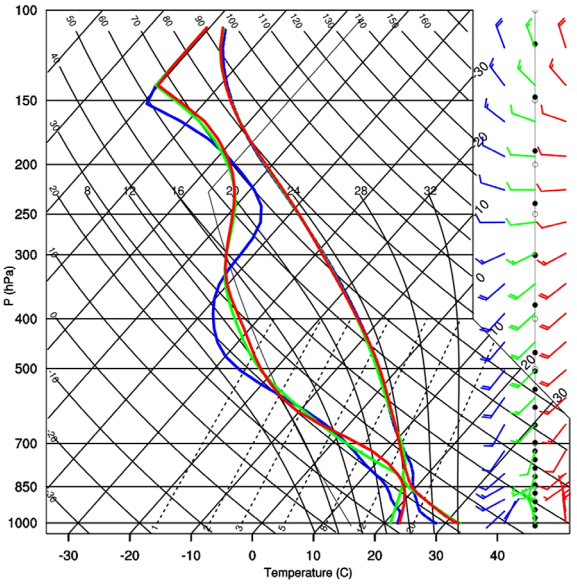

Fig. 10. Simulated soundings and wind profiles at the Banchiao station at 0800 (blue), 1100 (green), and 1200 (red) LST 14 June 2015.

are the mixing ratios of water vapor, cloud water, and rain water, respectively. Cold-pool propagation speed C defined in Rotunno et al. (1988) and Bryan and Parker (2010) is calculated using the vertical integral of buoyancy b as

$$C = \sqrt{-2\int_0^h b\,dz}, \tag{3}$$

where b is the buoyancy in Eq. (1) and h is the depth of the cold pool, which is defined as the height at which b first exceeds −0.05 m s^{-2}.

Figures 11 and 12 show the vertical structure and evolution of the sea breeze circulation from Danshui and the related convection initiation and development. The vertical cross sections are along the prevailing wind of SBD (northerly) after a 10-km horizontal average (see the N–S box in Fig. 9b for its horizontal location). The sea-breeze front accompanied by low-level updraft arrived at the foothill (x ~ 25 km) at 1200 LST, and the maximum low-level wind speed of the sea breeze (northerly) was 6 m s^{-1} (Fig. 11a).

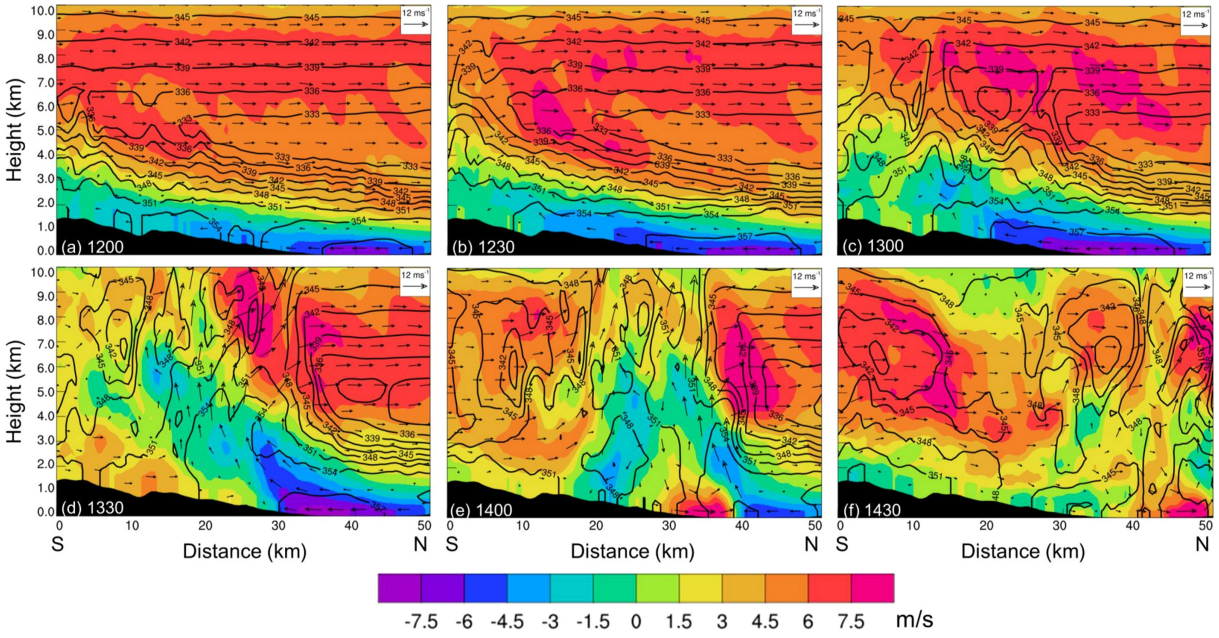

Fig. 11. Vertical cross sections showing the Danshui sea breeze: simulated meridional wind (colored; in units of m s^{-1}; positive for southerly and negative for northerly wind), equivalent potential temperature (black contours; in units of K), and along-plane vector: (a) 1200 LST, (b) 1230 LST, (c) 1300 LST, (d) 1330 LST, (e) 1400 LST, and (f) 1430 LST. The vertical cross sections are along the N–S direction of the rectangular box (after the 10-km average in zonal direction) in Fig. 9b. The averaged topography profile along the N–S cross section is shown by the black shading.

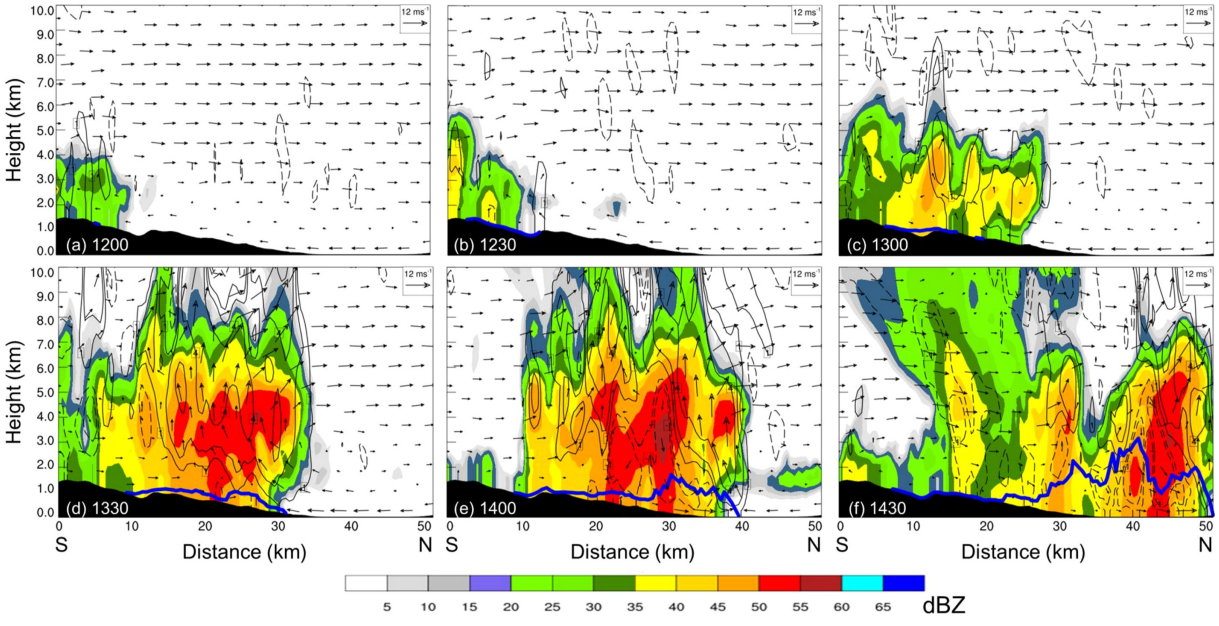

Fig. 12. As in Fig. 11, except for the simulated radar reflectivity (colored; in units of dBZ), vertical velocity (black contoured at −1, −0.5, 1, 2, 4, and 8 m s^{-1}; dashed for downdraft), and cold pool height (thick blue contour): (a) 1200 LST, (b) 1230 LST, (c) 1300 LST, (d) 1330 LST, (e) 1400 LST, and (f) 1430 LST.

Furthermore, the isolated convection occurred at the mountain peak at 1200 LST because of the upslope wind. After that, the sea breeze merged with the upslope wind, so it was hard to find the position of the sea breeze front. However, the region of high equivalent potential temperature ($\theta_e \geq 357$ K) still moved southward to the mountain slope (Figs. 11b, c). Because the moisture associated with the sea breeze was lifted by the terrain, another convection initiated at the mountain slope ($x \sim 20$ km) (Fig. 12c). Moreover, the isolated convection at the mountain peak gradually propagated northward with very shallow cold pool ($x \sim 10$ km) (Fig. 12c). Figures 11d and 12d show that the convection over the mountain slope evolved into the thunderstorm complex with a large extent of reflectivity greater than 40 dBZ ($x \sim 10-30$ km). The convectively generated outflow (southerly) and sea breeze (northerly) produced enhanced low-level convergence with a depth of about 1 km. The moisture associated with the sea breeze was forced to rise up over the cold pool and then condensed, releasing the potential instability (see the θ_e contour of 354 K reaching up to 5 km AGL in Fig. 11d). After 1400 LST (Figs. 11e, f, 12e, f), the cold-air outflow intensified with a maximum wind speed of 7.5 m s^{-1}, and the depth of the cold pool significantly elevated, with a maximum depth of 3 km because of the precipitation-induced latent cooling. The ATS system associated with the strong cold pool propagated northward to the basin plain, resulting in heavy rainfall in the commercial districts of Taipei City.

Figures 13 and 14 illustrate the vertical structure and evolution of the sea-breeze circulation from Keelung and its interaction with thunderstorm outflow. The vertical cross sections are along the prevailing wind of SBK (northeasterly) after a 10-km horizontal average (see the NE–SW box in Fig. 9b for its horizontal location). A comparison between the SBK and SBD at 1330 LST in Figs. 13d and 11d indicates that the SBK was weaker (i.e., with the maximum low-level wind speed of 6 m s^{-1}) than SBD (i.e., with the maximum low-level wind speed of 7.5 m s^{-1}) and that the SBK was dryer (i.e., with the highest low-level θ_e of 354 K) than SBD (i.e., with the highest low-level θ_e of 357 K). In addition, the thunderstorm outflow was relatively weak in the northeast direction (Figs. 13d–f), and the depth of the cold pool was lower than 1 km (Figs. 14d–f). As a result, the convergence between SBK and outflow was so weak that the cold pool could not lift the moisture effectively (see the 354-K θ_e contour reaching up to only 2 km AGL in Figs. 13d–f).

The Hovmöller diagrams along the SBD (Fig. 15) have the same horizontal dimension with the vertical cross sections in Figs. 11 and 12, which was along the prevailing wind of SBD (northerly) with a horizontal average of 10 km (see the N–S box in Fig. 9b). The Hovmöller diagram of meridional wind on the lowest model level (the 0.9965-eta level; about 35 m AGL) is shown in Fig. 15a. The Hovmöller diagram of most unstable convective available potential energy (MUCAPE) and the level of free convection (LFC) are shown in Figs. 15b and 15c, respectively. MUCAPE is the CAPE of parcel lifted from the level with the highest θ_e below 3 km AGL. Note that the "parcel" here refers to a "mean" parcel of 500-m depth, with the temperature and moisture averaged over that depth.

After 1000 LST, the SBD (> 3 m s^{-1}) established at the coastal region (25.1°N) and propagated southward with a speed of 4.6 m s^{-1} (estimated from the solid arrow in Fig. 15a). The upslope wind was established at the mountain slope (24.8–24.9°N) at about 0900 LST. As the SBD accompanied by abundant moisture expanded farther southward, the MUCAPE at the central basin and southern slope significantly increased (Fig. 15b). For example, the MUCAPE at the basin plain (25°N) increased from 200 J kg^{-1} at 0800 LST to 1600 J kg^{-1} at 1200 LST. On the other hand, the MUCAPE at the mountain region increased at 0800–1100 LST because of the enhanced solar heating. The convection which occurred at the mountain region at 1200–1300 LST (Figs. 8a–c) produced the cold pool with weak outflow (southerly) and shallow depth (Figs. 15a, c). After the convection evolved into the thunderstorm complex at 1330 LST (Figs. 8d–f), the cold outflow intensified to have a wind speed greater than 7.5 m s^{-1}, producing much stronger low-level convergence with the SBD (Fig. 15a). Moreover, the northward-propagation speed of the cold pool increased to about 6.3 m s^{-1} (estimated from the dashed arrow in Fig. 15a), and the passage of the cold pool resulted in a dramatic release of MUCAPE. Figure 15c may be used to explain the reason why the cold pool could release MUCAPE dramatically and maintained the subsequent convective development of the ATS system. After 1330 LST, the depth of the cold pool elevated to 1300 m, which was higher than the LFC of moist parcels of SBD (~ 1100 m) (Fig. 15c), so the cold pool could lift the moist air parcels up to LFC and then release their potential instabilities.

Next, let us compare the evolution of SBK to that of SBD. The Hovmöller diagrams along SBK (Fig. 16) have the same horizontal spatial dimension with the vertical cross sections in Figs. 13 and 14, which

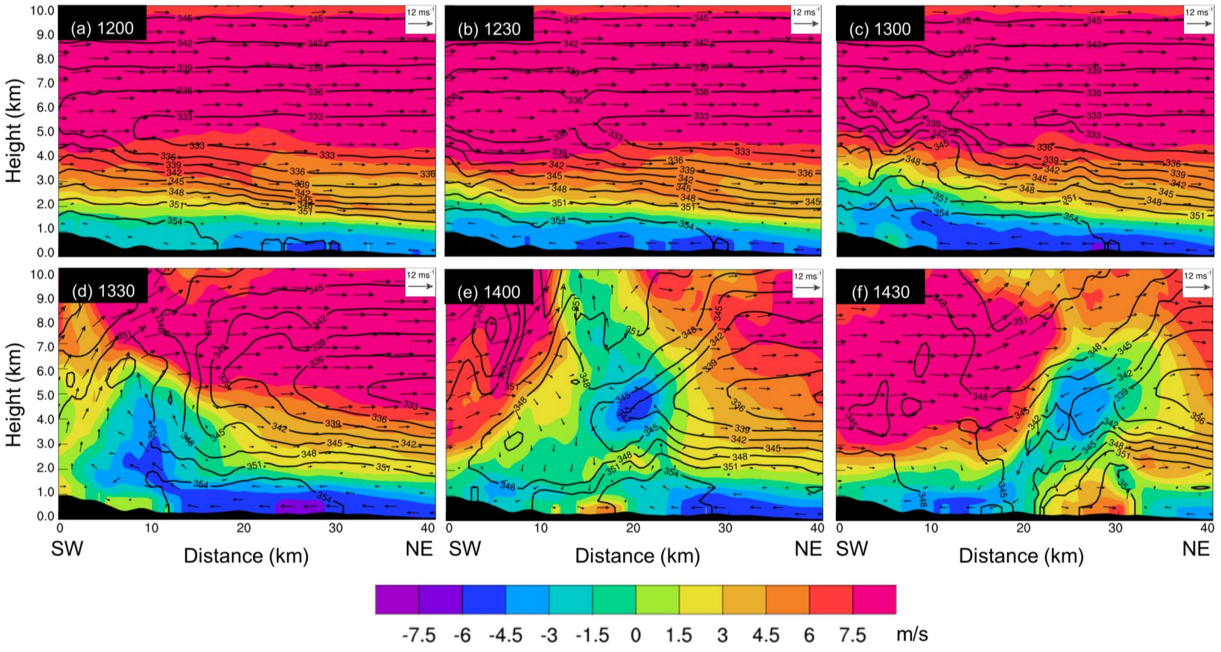

Fig. 13. Vertical cross sections showing the Keelung sea breeze: simulated along-plane wind (colored; in units of m s^{-1}; positive for southwesterly and negative for northeasterly wind), equivalent potential temperature (black contours; in units of K), and along-plane vector: (a) 1200 LST, (b) 1230 LST, (c) 1300 LST, (d) 1330 LST, (e) 1400 LST, and (f) 1430 LST. The vertical cross sections are along the NE–SW direction of the rectangular box (after the 10-km average in NW–SE direction) in Fig. 9b. The averaged topography profile along the NE–SW cross section is shown by the black shading.

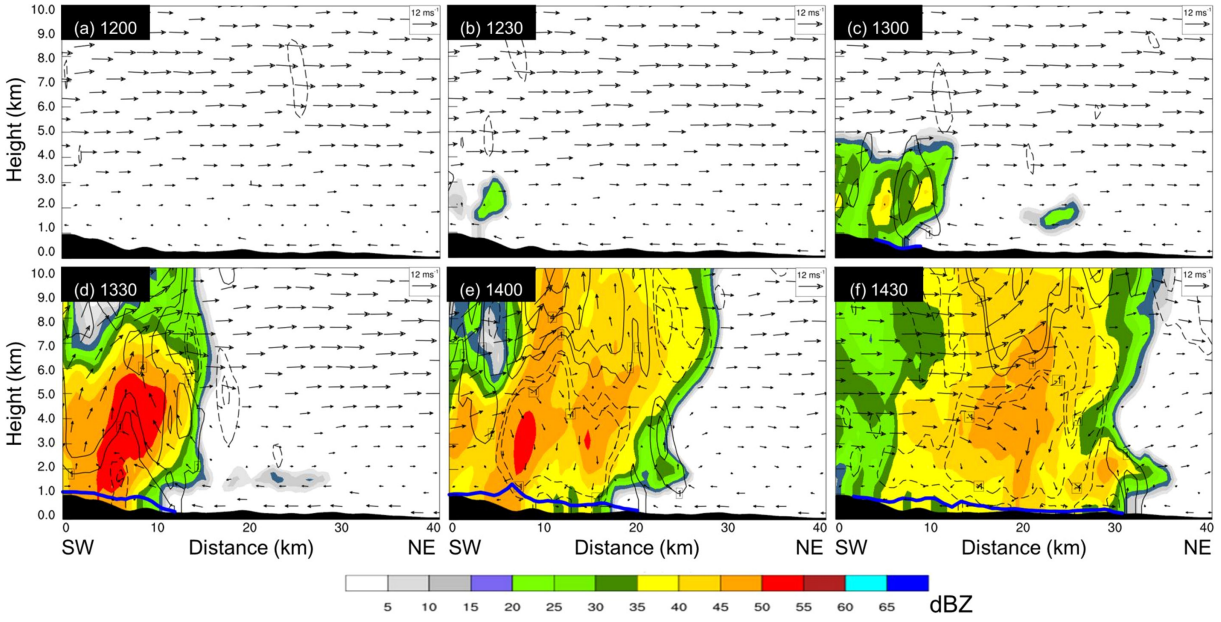

Fig. 14. As in Fig. 13, except for the simulated radar reflectivity (colored; in units of dBZ), vertical velocity (black contoured at −1, −0.5, 1, 2, 4, and 8 m s^{-1}; dashed for downdraft), and cold pool height (thick blue contour): (a) 1200 LST, (b) 1230 LST, (c) 1300 LST, (d) 1330 LST, (e) 1400 LST, and (f) 1430 LST.

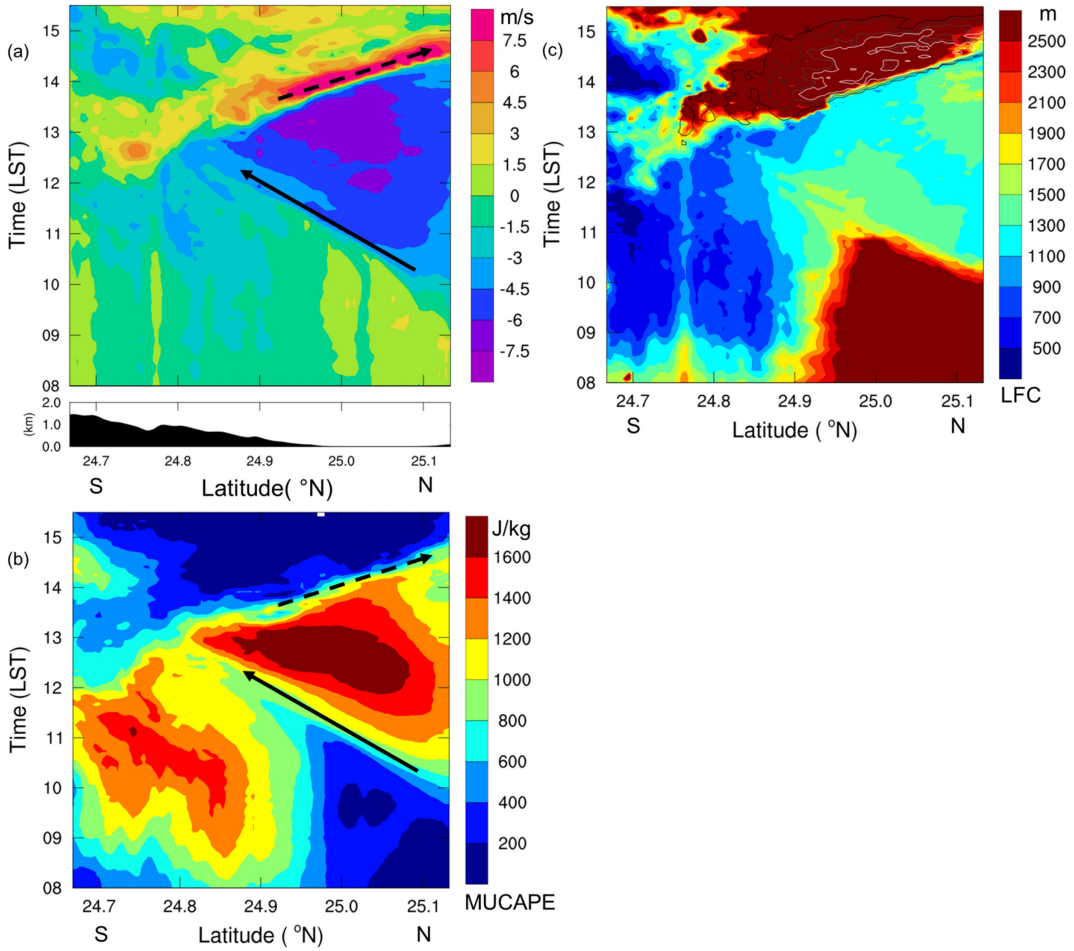

Fig. 15. Hovmöller diagrams of (a) meridional wind (colored; in units of m s^{-1}; positive for southerly and negative for northerly wind) at the 0.9965 eta-level; (b) most unstable convection available potential energy (MUCAPE) (colored; in units of J kg^{-1}); (c) level of free convection (LFC) (colored; in units of m) and cold pool height (contoured at 200, 500, 900, and 1300 m) along the Danshui sea-breeze circulation. The Hovmöller diagrams are along the N–S direction of the rectangular box (after the 10-km average in zonal direction) in Fig. 9b. The averaged topography profile is shown by black shading in (a).

was along the prevailing wind of SBK (northeasterly) with 10-km horizontal average (see the NE–SW box in Fig. 9b). A comparison between the SBD and SBK indicates that the near-surface wind speed of SBK was weaker (cf. Figs. 16a, 15a) and the MUCAPE of SBK was smaller (cf. Figs. 16b, 15b), which are consistent with previous discussions in Figs. 11–14. After 1400 LST, the depth of the gust front along the SBK in NE–SW orientation (< 500 m; Fig. 16c) was much shallower than that along the SBD in N–S orientation (~ 1300 m; Fig. 15c), so the gust front which collided with the SBK could not effectively lift the air parcels within the SBK to LFC (~ 1100 m). It appears that the convectively generated cold pool tends to propagate toward the area with the highest low-level θ_e and highest MUCAPE.

In summary, the SBD was fueled with more moisture and higher thermodynamic instability (MUCAPE) than the SBK. Moreover, the collision between the cold-air outflow and the SBD produced stronger dynamic forcing (low-level convergence), so convection inhibition could be overcome, and the MUCAPE associated with SBD could be fully released. These results suggest that the SBD played a major role in the development of ATS within the TB, whereas the SBK played a relatively minor role for this event.

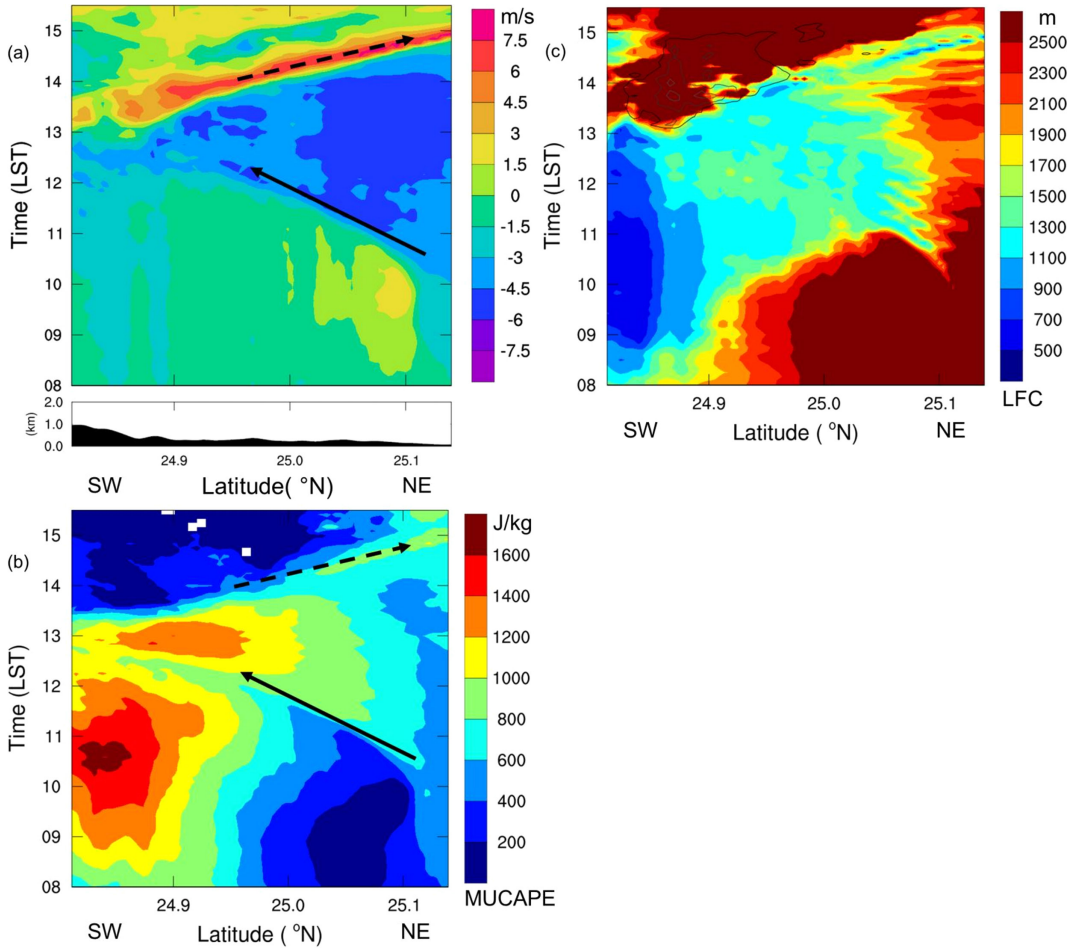

Fig. 16. Hovmöller diagrams of (a) along-sea-breeze wind (colored; in units of m s^{-1}; positive for southwesterly and negative for northeasterly wind) at the 0.9965 eta-level; (b) most unstable convection available potential energy (MUCAPE) (colored; in units of J kg^{-1}); (c) level of free convection (LFC) (colored; in units of m) and cold pool height (contoured at 200, 500, and 900 m) along the Keelung sea-breeze circulation. The Hovmöller diagrams are along the NE–SW direction of the rectangular box (after the 10-km average in NW–SE direction) in Fig. 9b. The averaged topography profile is shown by black shading in (a).

5.2 Sensitivity experiments on microphysics (NMLT and NEVP)

Figure 17 shows the simulated accumulated rainfall at 1200–1430 LST for the CNTL, NMLT, NEVP, and NDAT experiments. Note that the maximum rainfall within the whole TB and basin plain (terrain height < 100 m) is labeled on each panel. The simulated precipitation pattern between CNTL (Fig. 17a) and NMLT (Fig. 17b) was similar, except that the maximum rainfall within the basin plain in NMLT (74 mm) was smaller than that in CNTL (107 mm). The rainfall pattern between CNTL and NEVP (Fig. 17c) was very different. The maximum rainfall over the whole TB in NEVP was substantially shifted southward to the mountain peak (terrain height > 1300 m), with an accumulated amount (153 mm) more than that in CNTL (121 mm). Note that, as the evaporative cooling of rainwater is turned off in NEVP, the maximum rainfall at the basin plain where the commercial districts are located decreased dramatically to 26 mm, which is much less than that in CNTL.

To elucidate the physical mechanisms responsible for the heavy rainfall at the basin plain, Fig. 18 shows the horizontal and vertical cross sections of the ATS system at 1430 LST in the NMLT and NEVP experiments. Intense convection (with radar reflectivity

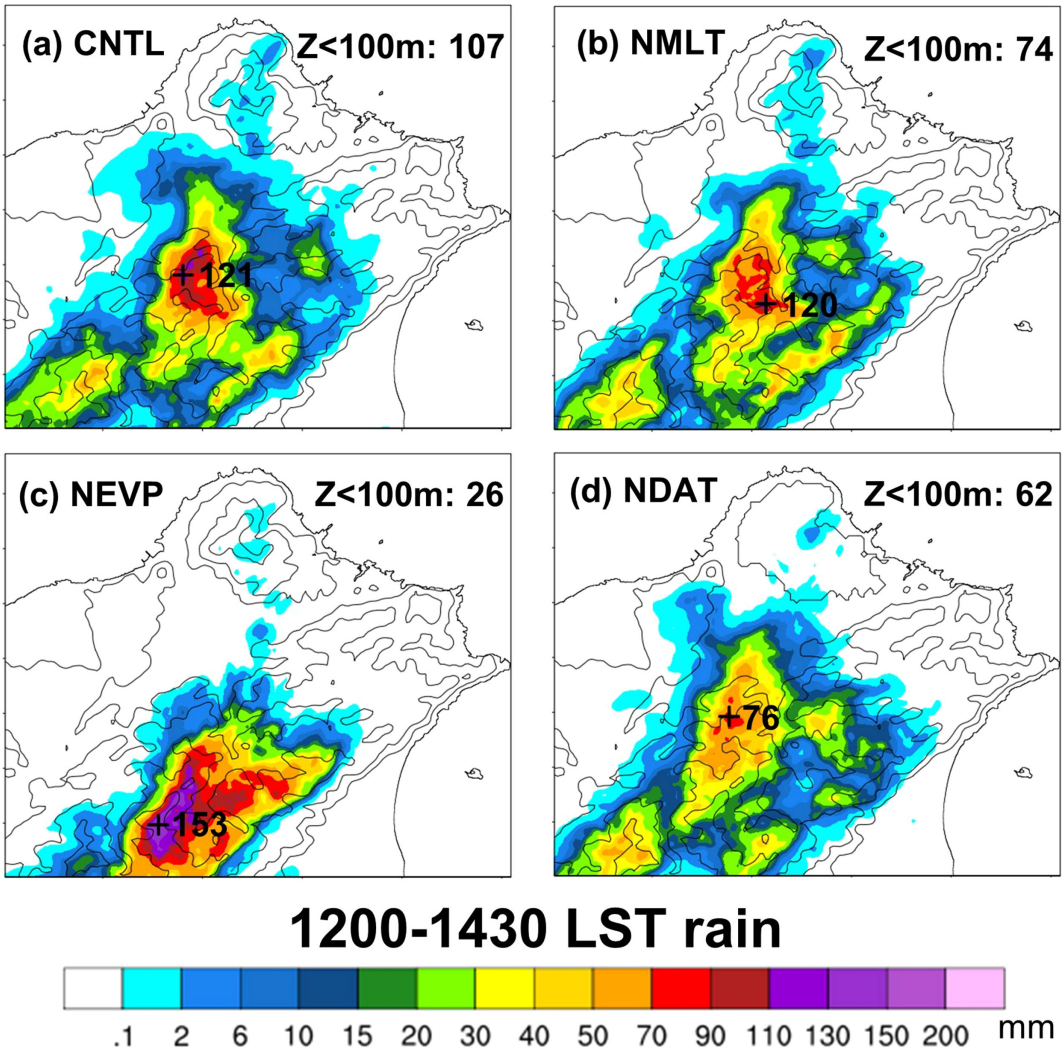

Fig. 17. 1200–1430 LST accumulated rainfall (in units of mm) from (a) CNTL, (b) NMLT, (c) NEVP, and (d) NDAT experiments. Black line is for the terrain height contoured at 100, 300, 700, and 1300 m. The location of the maximum accumulated precipitation within the Taipei Basin is denoted by the cross symbol in each panel. The maximum accumulated precipitation within the basin plain (terrain height $Z < 100$ m) is indicated at the upper right corner in each panel.

greater than 50 dBZ) propagated from the southern slope to the central basin and reached 25°5′N in the CNTL and NMLT runs (Figs. 8f, 18a). The vertical cross sections show that the convectively generated outflow (southerly) converged with the sea breeze (northerly) in the CNTL and NMLT runs, but the cold-pool depth in NMLT (with the maximum depth of 2.3 km) was shallower than that in CNTL (with the maximum depth of 3.3 km) at 1430 LST (cf. Figs. 12f, 18c).

Evaporative cooling of rainwater is turned off in the NEVP run, which basically eliminates the major mechanism for cold-pool generation by moist convection. In the absence of evaporative cooling, the intense convection was confined to the southern slope, and the sea breeze could still be found over the southern slope at 1430 LST in NEVP (Figs. 18b, d). Furthermore, the convection at the mountain slope was vigorous because of the continuous lifting of the sea breeze by the terrain, but it could not propagate to the basin plain as CNTL (cf. Figs. 12f, 18d). These results indicate that the cold-pool dynamics was essential for the heavy

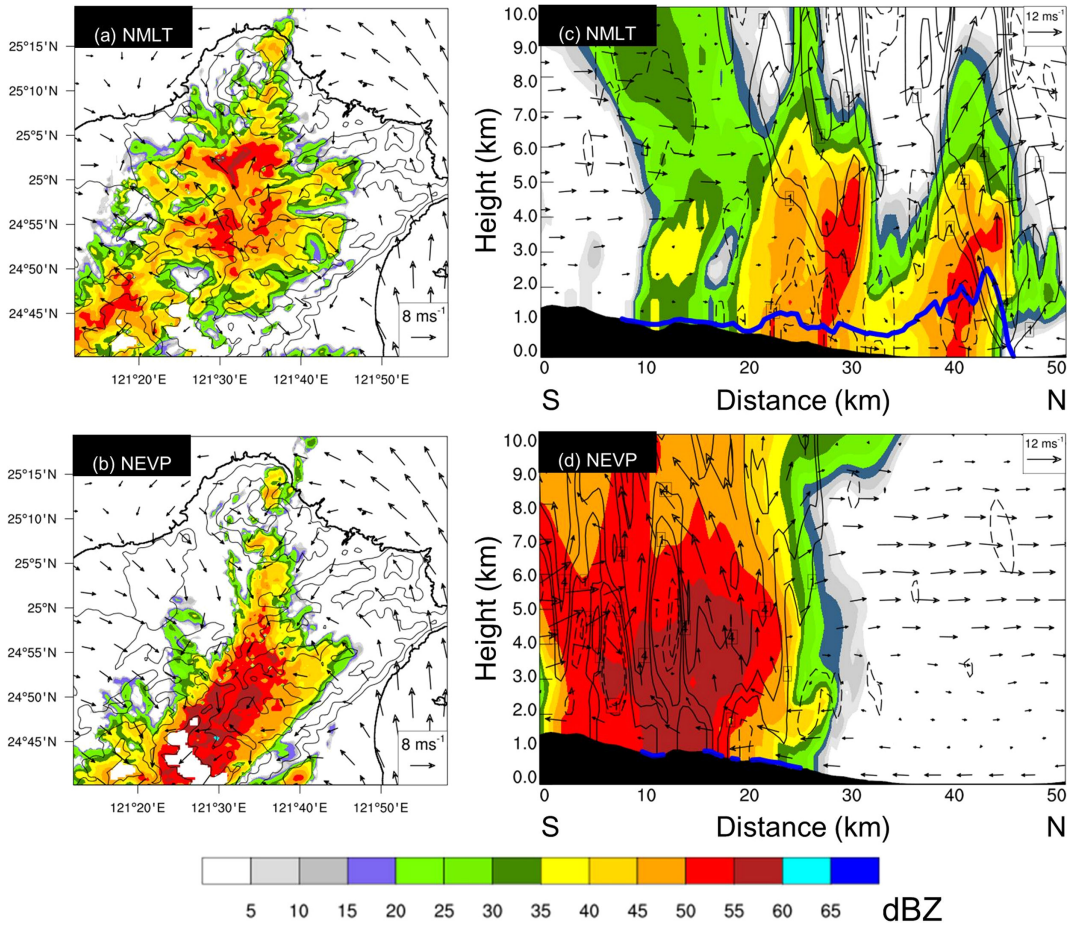

Fig. 18. (a), (b) As in Fig. 8f but for the results from the (a) NMLT and (b) NEVP experiments at 1430 LST. (c), (d) As in Fig. 12f but for the results from the (c) NMLT and (d) NEVP experiments at 1430 LST.

rainfall within the basin plain.

The Hovmöller diagrams of 35-m meridional wind and MUCAPE of NMLT and NEVP are shown in Fig. 19. In CNTL, the northward-propagation speed of the gust front was 6.3 m s^{-1}, and the passage of the gust front resulted in a dramatic release of MUCAPE. In NMLT, the northward-propagation speed of the gust front was 5.3 m s^{-1} (estimated from the dashed arrow in Fig. 19a), which was slightly slower than that in CNTL, since the melting cooling of graupel was turned off in NMLT. A subtle difference between the outflow structure in CNTL and NMLT (cf. Figs. 15a, 19a) was that the outflow in NMLT had two wind speed maxima (one at the gust front and the other behind the gust front), with a slightly weaker wind speed at the gust front than that in CNTL. Therefore, the low-level convergence produced by the outflow and sea breeze in NMLT was weaker, resulting in a less release of MUCAPE after the passage of the gust front (cf. the dashed arrows in Figs. 15b, 19b) and less rainfall at the basin plain.

In the absence of evaporative cooling, the sea breeze continuously advanced southward to the southern slope in NEVP (Fig. 19c), and the MUCAPE within the central basin (24.9°N to 25.1°N) could not be released. As a result, the rainfall within the basin plain in NEVP was much weaker than those in CNTL and NMLT.

The evolution of cold-pool characteristics averaged over the TB domain (Fig. 8d) from 1230 LST to 1500 LST is shown in Fig. 20. The temporal-average values for three experiments over 1230–1500 LST are also shown on each panel. It is clear from Fig. 20a that the cold pool in NMLT was slightly weaker than that in CNTL, and the cold pool in NEVP was much weaker than those in CNTL and NMTL. For the time-average

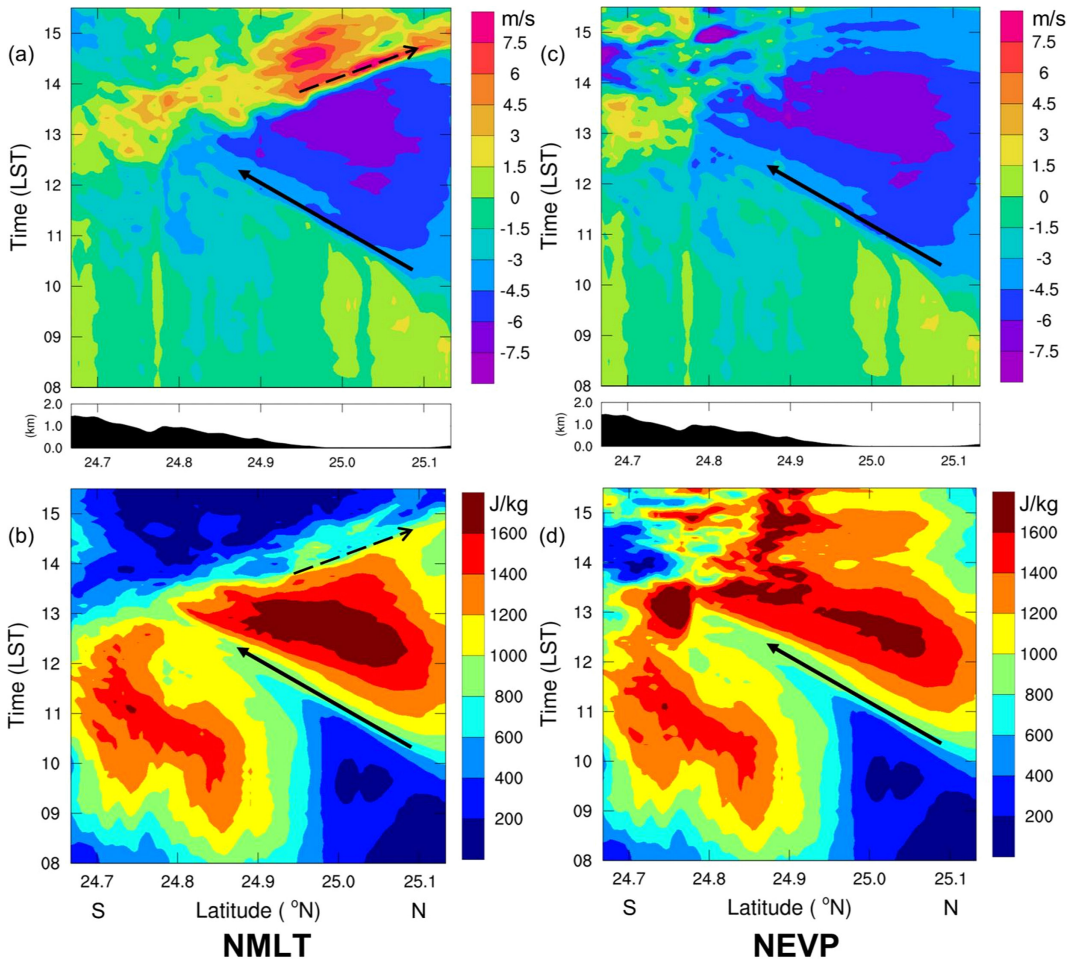

Fig. 19. (a), (b) As in Figs. 15a and 15b but for the results from the NMLT experiment. (c), (d) As in Figs. 15a and 15b but for the results from the NEVP experiment.

value, the cold-pool speed is deceased by 38 % if no evaporative cooling of rainwater (Fig. 20c) and decreased by 13 % if no melting cooling of graupel.

To sum up, evaporative cooling of rainwater played a major role in the propagation and intensification of cold-air outflow, whereas melting cooling of graupel only played a minor role. In the absence of evaporative cooling of rainwater, the intense convection cannot propagate from the mountain slope to the central basin, and the rainfall within the basin plain is decreased substantially.

5.3 Sensitivity experiment on local terrain (NDAT)

In the NDAT experiment where the local terrain of Mount Datun north of TB was removed, the rainfall significantly decreased (Figs. 17a, d). Figure 21 shows the comparison of 10-m horizontal wind speed between CNTL and NDAT. Because the CNTL experiment suggests that the SBD played a major role in the development of ATS within the TB, we focus on the SBD. It is clear that the wind speed of SBD intensified after passing through the Danshui River Valley between Mount Datun and Mount Guanyin (Fig. 21a). In the absence of Mount Datun, the wind speed of SBD significantly decreased (compare the wind speeds over the dashed circles in Figs. 21a, b). To elucidate the impact of Mount Datun on the sea breeze circulation and its related rainfall, we further compare the difference of SBD characteristics between CNTL and NDAT (Fig. 22). Note that a 7-min time difference between the CNTL (Figs. 22a, d) and NDAT (Figs. 22b, e) is used to adjust the timing difference of the movement of the sea-breeze front accompanied by low-level updraft. Figure 22c shows the difference

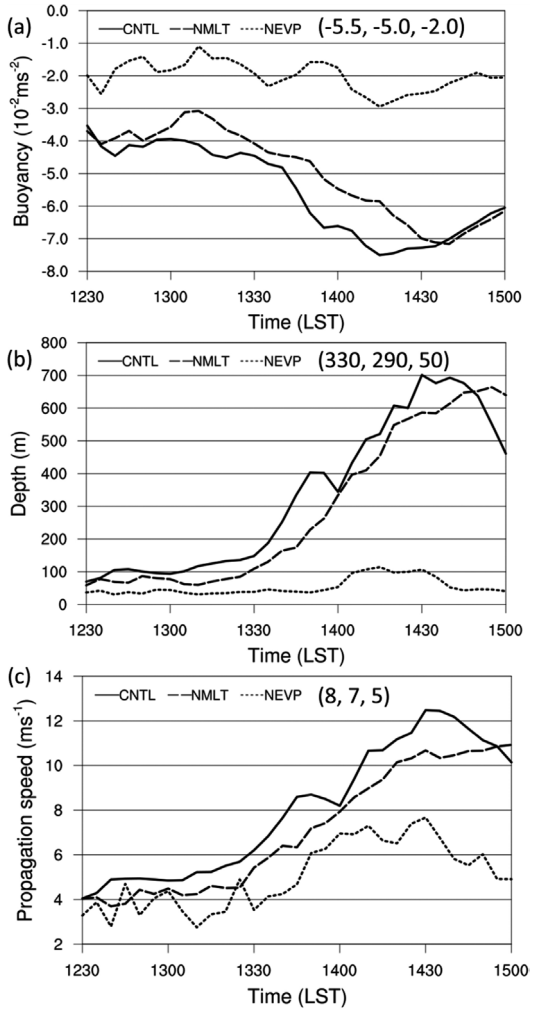

Fig. 20. Time series of domain-averaged (a) near-surface (35 m) buoyancy (in units of 10^{-2} m s^{-2}), (b) cold-pool depth (in units of m), and (c) cold-pool propagation speed (in units of m s^{-1}) from the CNTL (solid), NMLT (long dash), and NEVP (short dash) runs. The domain is for the rectangular box in Fig. 8d. The temporal-averaged values over 1230–1500 LST in CNTL, NMLT, and NEVP are also shown on each panel.

in the wind fields between the CNTL and NDAT experiments along the cross section shown in Figs. 22a, b. The sea breeze in CNTL was stronger than that in NDAT, with a low-level wind speed difference of 0.8 m s^{-1} near the sea-breeze front. The local topography of Mount Datun produced the channel effect along Danshui River Valley and intensified sea-breeze circulation. In the absence of Mount Datun, the channel effect and the sea breeze significantly weakened.

On the other hand, the CAPE contour of 900 J kg^{-1} nearly overlapped with the 354-K θ_e contour (Figs. 22d, e), indicating that they were positively correlated at low levels. The distance between the sea-breeze front and the near-surface 354-K θ_e contour (or 900-J kg^{-1} CAPE contour) in NDAT was 5 km (Fig. 22e), which was longer than CNTL (3 km; see Fig. 22d). Figure 22f shows the difference in CAPE between the CNTL and NDAT experiments along the cross section shown in Figs. 22d, e. The CAPE associated with the sea breeze in CNTL was stronger than that in NDAT,

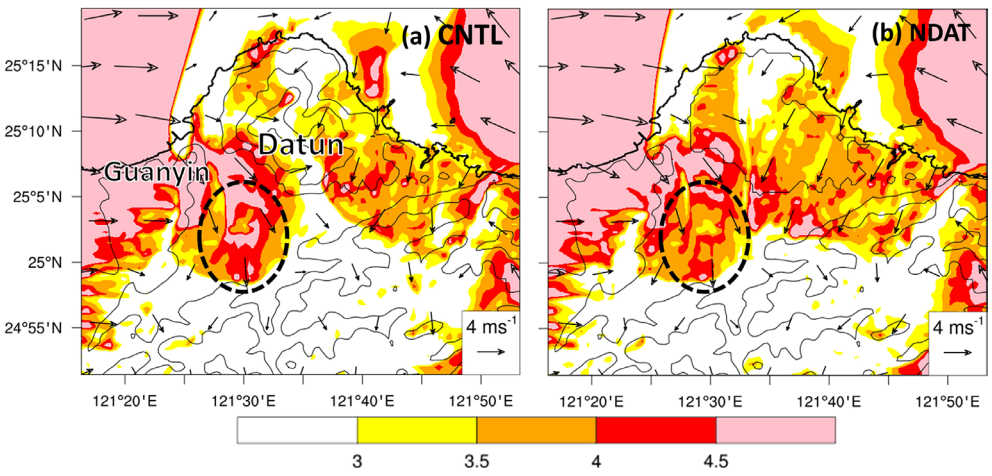

Fig. 21. Horizontal cross sections of 10-m horizontal wind speed (colored; in units of m s^{-1}) and 10-m wind vectors at (a) 1113 LST in the CNTL run and (b) 1120 LST in the NDAT run. Black line is for the terrain height contoured at 100, 300, 700, and 1300 m. Mount Datun and Mount Guanyin are labeled in (a).

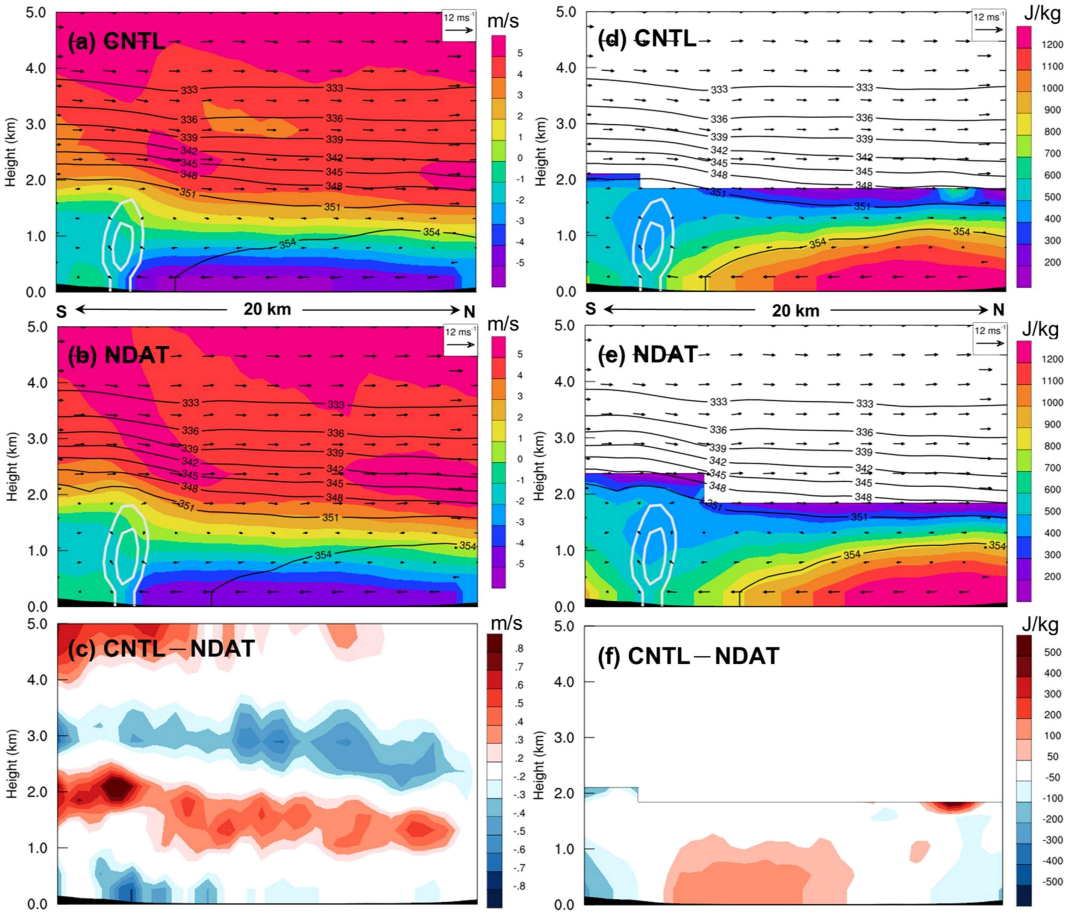

Fig. 22. Vertical cross sections along the Danshui sea breeze: (a), (b) simulated meridional wind (colored; in units of m s^{-1}; positive for southerly and negative for northerly wind), equivalent potential temperature (black contours; in units of K), updraft (gray contours, 0.5, 1 m s^{-1}), and along-plane vector at (a) 1113 LST in the CNTL run and (b) 1120 LST in the NDAT run. (c) Difference between (a) and (b) (CNTL minus NDAT). (d), (e) Simulated CAPE (colored; in units of J kg^{-1}), equivalent potential temperature (black contours; in units of K), updraft (gray contours, 0.5, 1 m s^{-1}), and along-plane vector at (d) 1113 LST in the CNTL run and (e) 1120 LST in the NDAT run. (f) Difference between (d) and (e) (CNTL minus NDAT). The vertical cross sections have the same horizontal spatial dimension with the northern part of the vertical cross sections (x = 30–50 km) in Fig. 11. Note that the vertical scale is up to 5 km.

with a CAPE difference of 200 J kg^{-1}. In the absence of Mount Datun, the thermodynamic instability (moisture) associated with the sea breeze significantly decreased.

These results suggest that the local topography of Mount Datun may produce the channel effect along Danshui River Valley, intensify sea-breeze circulation, and transport more moisture into the TB. This terrain-induced modification of the sea breeze circulation made its dynamic and thermodynamic characteristics more favorable for convection development, resulting in a stronger ATS system with heavier rainfall within Taipei City.

6. Conclusions

In this study, a severe ATS event associated with an intense rainfall rate (131 mm h^{-1}) that developed within the TB on 14 June 2015 was investigated. A high-resolution WRF simulation with the horizontal grid size nested down to 0.5 km was conducted to capture the evolution of the ATS system and sea-breeze circulation of this event, with reasonable agreement with the observations.

The CNTL simulation results show that the CAPE

was increased from 800 to 3200 J kg^{-1} with abundant moisture transport by the sea breeze from 08 to 12 LST, fueling large thermodynamic instability for the development of the ATS. Moreover, the SBD, which was much more humid than that from the SBK, supplied more convective instability.

It is found that convection was initiated by the upslope wind from the valley at the mountain peak and by the sea breeze at the foothill. After the onset of convection, the scattered convective cells at the southern slope merged into the severe thunderstorm complex with a large area of radar reflectivity greater than 40 dBZ, and the depth of the cold pool was elevated to 1300 m, which was higher than the LFC for the most unstable air parcel from the sea breeze (1100 m). The collision between the convection outflow (southerly) and sea breeze (northerly) produced the enhanced low-level convergence. As the cold pool collided with the sea breeze and lifted the moist parcels up to LFC, substantial MUCAPE could be released dramatically by overcoming convection inhibition, resulting in the subsequent development of the ATS system.

Sensitivity experiments on cloud microphysics indicate that evaporative cooling of rainwater played a major role in the propagation and intensification of cold-air outflow, whereas melting cooling of graupel played a relatively minor role. In the absence of evaporative cooling of rainwater, the intense convection (with radar reflectivity greater than 50 dBZ) could not propagate from the southern slope to the central basin, and the rainfall within the basin plain (terrain height < 100 m) decreased dramatically.

A sensitivity experiment on the local topography (Mount Datun) at the coastal region shows that the local terrain of Mount Datun may produce the channel effect along Danshui River Valley, intensify sea-breeze circulation, and transport more moisture. This terrain-induced modification of sea-breeze circulation makes its dynamic and thermodynamic characteristics more favorable for convection development, resulting in a stronger ATS system with heavier rainfall within the TB. To summarize our major findings in this study, Fig. 23 is the schematic diagram illustrating the interactions between the sea breeze, cold pool, and coastal terrain for the development of the ATS within the TB on 14 June 2015.

Although the control numerical simulation in this study bears close resemblance with the radar and surface observations, we should keep in mind that the conclusions obtained from this modeling study are mainly based on a numerical simulation with model deficiencies, physics uncertainties, and numerical errors. More ATS cases in other geographic locations or under different synoptic settings should be investigated in the future to verify or revise the conclusions obtained from this case study.

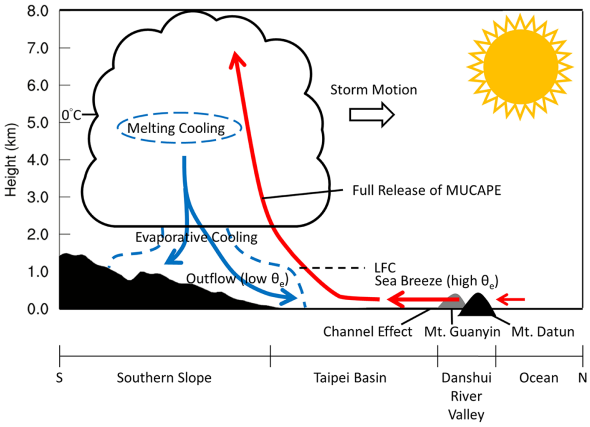

Fig. 23. Schematic diagram of the interactions between the sea breeze, cold pool, and coastal terrain for the development of the afternoon thunderstorm over the Taipei Basin.

Acknowledgments

Constructive comments by the reviewers and Editor Dr. Masayuki Kawashima on our manuscript are highly appreciated. We thank the Central Weather Bureau in Taiwan for providing the observation data. Parts of the results were from the first author's M.S. thesis study at National Taiwan University. This work was supported by the Ministry of Science and Technology in Taiwan under Grants MOST 107-2625-M-002-009 and MOST 108-2111-M-002-011-MY2.

Appendix: Definition of the basic state

The definition of buoyancy highly depends on the basic state, so it is essential to define the basic state for convection. There are two different ways to define basic state (for example, see Eq. (1) in the text for the definition of buoyancy in terms of virtual potential temperature). One way is to define basic state as the atmospheric state in a pre-convection environment, i.e., the ambient thermodynamics state before the ATS convection occurs, and it is time-invariant. Thus, one can select the sounding at the model initial time as the pre-convection environmental condition. The other way is to define the basic state as the horizontal mean state of the environment where the thunderstorm convection take places, so the basic state is a function of time. The time-invariant condition in a pre-convection

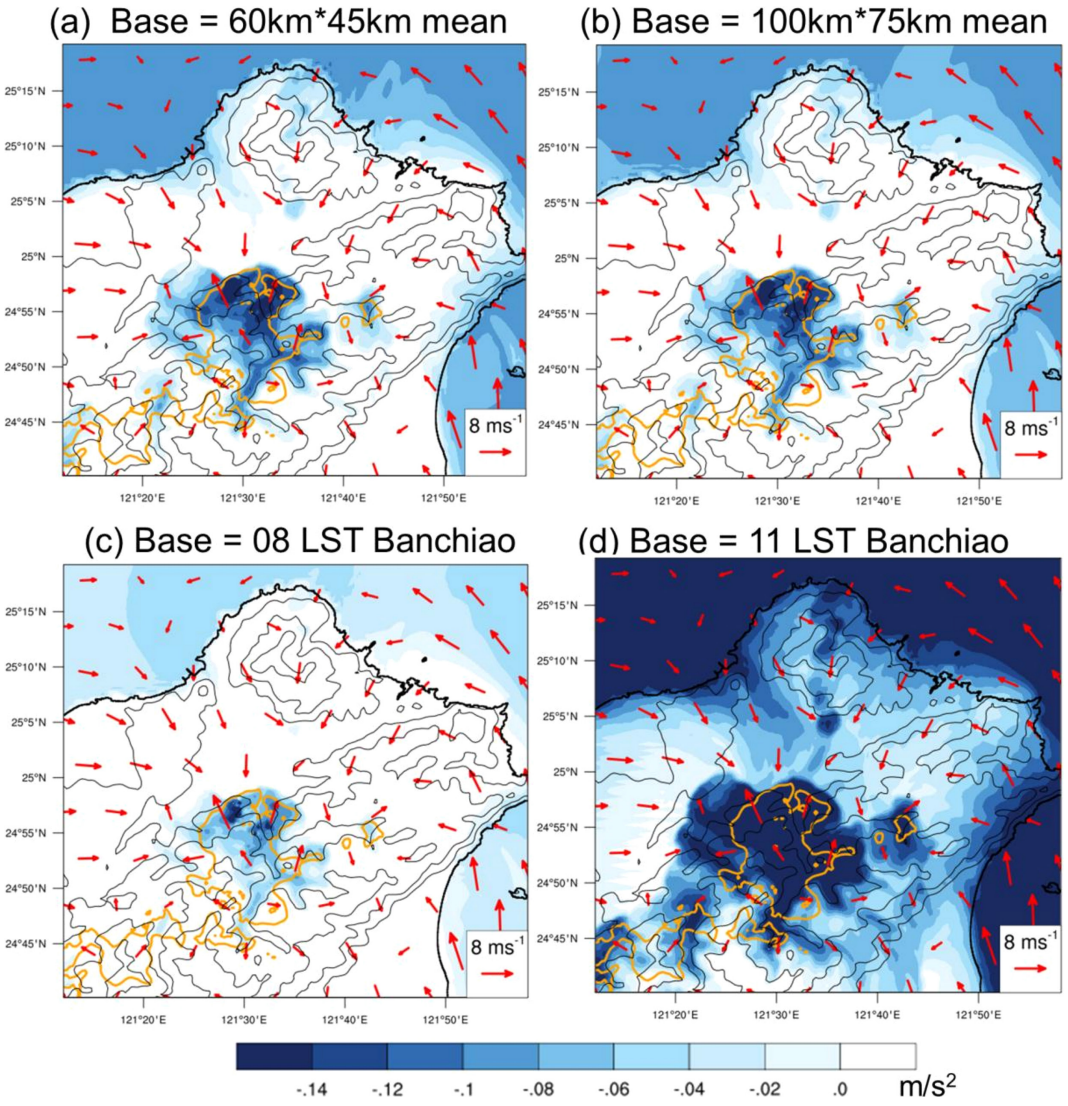

Fig. A. Horizontal cross sections of 35-m buoyancy (colored; in units of m s^{-2}), 35-m rainwater mixing ratio (orange contoured; 1 g kg^{-1}), and 10-m wind vectors from the CNTL simulation at 1350 LST: Basic state is (a) the domain mean within the rectangular area centered at the Taipei Basin (with a size of 60 km by 45 km; see the bold box in Fig. 8d); (b) the domain mean within the rectangular area centered at the Taipei Basin (with a size of 100 km by 75 km); (c) Banchiao sounding at 0800 LST; (d) Banchiao sounding at 1100 LST. Black line is for the terrain height contoured at 100, 300, 700, and 1300 m.

environment was widely used in the idealized simulations in the literature in which the thermodynamics condition, surface condition, and wind field were assumed horizontally homogeneous in most idealized simulations. However, the environmental conditions are not horizontally homogeneous in real cases. Moreover, longwave and shortwave radiations are included in real-case simulations. Therefore, in our real-case study, it may be more appropriate to use the second definition, i.e., the horizontal mean state of the ambient environment with embedded thunderstorms, as the basic state. Thus, in our study, we use the second definition to define the basic state as the domain-mean state within the TB area.

Figure A above shows the horizontal distribution of buoyancy, rainwater mixing ratio, and wind vectors near the surface for different definitions of basic state conditions. It clearly displays that the buoyancy field

defined using the second definition of horizontal-mean state (see Figs. Aa, b) corresponds well to the surface rainfall pattern (in orange contour). On the other hand, the buoyancy field defined using the first definition of the time-invariant pre-convection state (see Figs. Ac, d) corresponds poorly to the surface rainfall, particularly for Fig. Ad, with the pre-convection state just only 3 h before the occurrence of thunderstorm rainfall. Hence, Fig. A supports our usage of the horizontal-mean state as the basic state for buoyancy calculation and for basic state for "cold-pool height" and "cold-pool propagation speed".

References

Baker, R. D., B. H. Lynn, A. Boone, W-K. Tao, and J. Simpson, 2001: The influence of soil moisture, coastline curvature, and land-breeze circulations on sea-breeze-initiated precipitation. *J. Hydrometeor.*, **2**, 193–211.

Bryan, G. H., and M. D. Parker, 2010: Observations of a squall line and its near environment using high-frequency Rawinsonde launches during VORTEX2. *Mon. Wea. Rev.*, **138**, 4076–4097.

Chen, G. T.-J., H.-C. Chou, T. C. Chang, and C. S. Liu, 2001: Frontal and non-frontal convection over northern Taiwan in mei-yu season. *Atmos. Sci.*, **29**, 37–52 (in Chinese with English abstract).

Chen, T.-C., S.-Y. Wang, and M.-C. Yen, 2007: Enhancement of afternoon thunderstorm activity by urbanization in a valley: Taipei. *J. Appl. Meteor. Climatol.*, **46**, 1324–1340.

Chen, T.-C., M.-C. Yen, J.-D. Tsay, C.-C. Liao, and E. S. Takle, 2014: Impact of afternoon thunderstorms on the land-sea breeze in the Taipei basin during summer: An experiment. *J. Appl. Meteor. Climatol.*, **53**, 1714–1738.

Chen, X., K. Zhao, M. Xue, B. Zhou, X. Huang, and W. Xu, 2015: Radar-observed diurnal cycle and propagation of convection over the Pearl River Delta during Mei-Yu season. *J. Geophys. Res.*, **120**, 12557–12575.

Chen, X., F. Zhang, and K. Zhao, 2016: Diurnal variations of the land–sea breeze and its related precipitation over south China. *J. Atmos. Sci.*, **73**, 4793–4815.

Chen, Y.-L., and J. Li, 1995: Characteristics of surface airflow and pressure patterns over the island of Taiwan during TAMEX. *Mon. Wea. Rev.*, **123**, 695–716.

Dee, D. P., S. M. Uppala, A. J. Simmons, P. Berrisford, P. Poli, S. Kobayashi, U. Andrae, M. A. Balmaseda, G. Balsamo, P. Bauer, P. Bechtold, A. C. M. Beljaars, L. van de Berg, J. Bidlot, N. Bormann, C. Delsol, R. Dragani, M. Fuentes, A. J. Geer, L. Haimberger, S. B. Healy, H. Hersbach, E. V. Hólm, L. Isaksen, P. Kållberg, M. Köhler, M. Matricardi, A. P. McNally, B. M. Monge-Sanz, J.-J. Morcrette, B.-K. Park, C. Peubey, P. de Rosnay, C. Tavolato, J.-N. Thépaut, and F. Vitart, 2011: The ERA-Interim reanalysis: Configuration and performance of the data assimilation system. *Quart. J. Roy. Meteor. Soc.*, **137**, 553–597.

Dudhia, J., 1989: Numerical study of convection observed during the winter monsoon experiment using a mesoscale two-dimensional model. *J. Atmos. Sci.*, **46**, 3077–3107.

Feng, Z., S. Hagos, A. K. Rowe, C. D. Burleyson, M. N. Martini, and S. P. de Szoeke, 2015: Mechanisms of convective cloud organization by cold pools over tropical warm ocean during the AMIE/DYNAMO field campaign. *J. Adv. Model. Earth Syst.*, **7**, 357–381.

Hanna, S. R., and R. Yang, 2001: Evaluations of mesoscale models' simulations of near-surface winds, temperature gradients, and mixing depths. *J. Appl. Meteor.*, **40**, 1095–1104.

Helmus, J. J., and S. M. Collis, 2016: The Python ARM Radar Toolkit (Py-ART), a library for working with weather radar data in the python programming language. *J. Open Res. Software,* **4**, e25, doi:10.5334/jors.119.

Hong, S.-Y., and H.-L. Pan, 1996: Nonlocal boundary layer vertical diffusion in a medium-range forecast model. *Mon. Wea. Rev.*, **124**, 2322–2339.

Huang, Y., Y. Liu, Y. Liu, H. Li, and J. C. Knievel, 2019: Mechanisms for a record-breaking rainfall in the coastal metropolitan city of Guangzhou, China: Observation analysis and nested very large eddy simulation with the WRF model. *J. Geophys. Res.*, **124**, 1370–1391.

Johnson, R. H., and J. F. Breach, 1991: Diagnosed characteristics of precipitation systems over Taiwan during the May-June 1987 TAMEX. *Mon. Wea. Rev.*, **119**, 2540–2557.

Jou, B. J.-D., 1994: Mountain-originated mesoscale precipitation system in northern Taiwan: A case study of 21 June 1991. *Terr. Atmos. Oceanic Sci.*, **5**, 169–197.

Jou, B. J.-D., Y.-C. Kao, R.-G. R. Hsiu, C.-J. U. Jung, J. R. Lee, and H. C. Kuo, 2016: Observational characteristics and forecast challenge of Taipei flash flood afternoon thunderstorm: Case study of 14 June 2015. *Atmos. Sci.*, **44**, 57–82 (in Chinese with English abstract).

Kain, J. S., and J. M. Fritsch, 1993: Convective parameterization for mesoscale models: The Kain-Fritsch scheme. *The Representation of Cumulus Convection in Numerical Models*. Emanuel, K. A., and D. J. Raymond (eds.), Meteor. Monogr., No. 46, Amer. Meteor. Soc., 165–170 pp.

Kerns, B. W. J., Y. L. Chen, and M. Y. Chang, 2010: The diurnal cycle of winds, rain, and clouds over Taiwan during the mei-yu, summer, and autumn rainfall regimes. *Mon. Wea. Rev.*, **138**, 497–516.

Kuo, K.-T., and C.-M. Wu, 2019: The precipitation hotspots of afternoon thunderstorms over the Taipei Basin: Idealized numerical simulations. *J. Meteor. Soc. Japan*, **97**, 501–517.

Lim, K.-S. S., and S.-Y. Hong, 2010: Development of an effective double-moment cloud microphysics scheme with prognostic cloud condensation nuclei (CCN) for weather and climate models. *Mon. Wea. Rev.*, **138**, 1587–1612.

Lin, P.-F., P.-L. Chang, B. J.-D. Jou, J. W. Wilson, and R. D. Roberts, 2011: Warm season afternoon thunderstorm characteristics under weak synoptic-scale forcing over Taiwan Island. *Wea. Forecasting*, **26**, 44–60.

Liu, Y., T. T. Warner, E. G. Astling, J. F. Bowers, C. A. Davis, S. F. Halvorson, D. L. Rife, R.-S. Sheu, S. P. Swerdlin, and M. Xu, 2008: The operational mesogamma-scale analysis and forecast system of the U.S. Army Test and Evaluation Command. Part II: Interrange comparison of the accuracy of model analyses and forecasts. *J. Appl. Meteor. Climatol.*, **47**, 1093–1104.

Miao, J.-E., and M.-J. Yang, 2018: Cell merger and heavy rainfall of the severe afternoon thunderstorm event at Taipei on 14 June 2015. *Atmos. Sci.*, **46**, 427–453 (in Chinese with English abstract).

Mlawer, E. J., S. J. Taubman, P. D. Brown, M. J. Iocono, and S. A. Clough, 1997: Radiative transfer for inhomogeneous atmospheres: RRTM, a validated correlated-k model for the longwave. *J. Geophys. Res.*, **102**, 16663–16682.

Rotunno, R., J. B. Klemp, and M. L. Weisman, 1988: A theory for strong, long-lived squall lines. *J. Atmos. Sci.*, **45**, 463–485.

Skamarock, W. C., J. B. Klemp, J. Dudhia, D. O. Gill, D. M. Barker, M. G. Duda, X.-Y. Huang, W. Wang, and J. G. Powers, 2008: *A description of the Advanced Research WRF version 3*. NCAR Tech. Note NCAR/TN-4751STR, 113 pp.

Tompkins, 2001: Organization of tropical convection in low vertical wind shears: The role of cold pools. *J. Atmos. Sci.*, **58**, 1650–1672.

Wang, C.-C., and D. J. Kirshbaum, 2017: Idealized simulations of sea breezes over mountainous islands. *Quart. J. Roy. Meteor. Soc.*, **143**, 1657–1669.

Yang, M.-J., and R. A. Houze, Jr., 1995: Sensitivity of squall-line rear inflow to ice microphysics and environmental humidity. *Mon. Wea. Rev.*, **123**, 3175–3193.